

# A Unifying Principle for the Functional Organization of Visual Cortex

Eshed Margalit<sup>1,✉</sup>, Hyodong Lee<sup>2</sup>, Dawn Finzi<sup>3,4</sup>, James J. DiCarlo<sup>2,5,6</sup>, Kalanit Grill-Spector<sup>3,7,\*</sup>, and Daniel L. K. Yamins<sup>3,4,7,\*</sup>

<sup>1</sup>Neurosciences Graduate Program, Stanford University, Stanford, CA 94305

<sup>2</sup>Department of Brain and Cognitive Sciences, Massachusetts Institute of Technology, Cambridge, MA 02139

<sup>3</sup>Department of Psychology, Stanford University, Stanford, CA 94305

<sup>4</sup>Department of Computer Science, Stanford University, Stanford, CA 94305

<sup>5</sup>McGovern Institute for Brain Research, Massachusetts Institute of Technology, Cambridge, MA 02139

<sup>6</sup>Center for Brains Minds and Machines, Massachusetts Institute of Technology, Cambridge, MA 02139

<sup>7</sup>Wu Tsai Neurosciences Institute, Stanford University, Stanford, CA 94305

\* co-senior author

**A key feature of many cortical systems is functional organization: the arrangement of neurons with specific functional properties in characteristic spatial patterns across the cortical surface. However, the principles underlying the emergence and utility of functional organization are poorly understood. Here we develop the Topographic Deep Artificial Neural Network (TDANN), the first unified model to accurately predict the functional organization of multiple cortical areas in the primate visual system. We analyze the key factors responsible for the TDANN's success and find that it strikes a balance between two specific objectives: achieving a task-general sensory representation that is self-supervised, and maximizing the smoothness of responses across the cortical sheet according to a metric that scales relative to cortical surface area. In turn, the representations learned by the TDANN are lower dimensional and more brain-like than those in models that lack a spatial smoothness constraint. Finally, we provide evidence that the TDANN's functional organization balances performance with inter-area connection length, and use the resulting models for a proof-of-principle optimization of cortical prosthetic design. Our results thus offer a unified principle for understanding functional organization and a novel view of the functional role of the visual system in particular.**

Correspondence: [eshed.margalit@gmail.com](mailto:eshed.margalit@gmail.com)

## 28 Introduction

29 Neurons in sensory cortical systems support two kinds of measurements: their response patterns as a function  
30 of stimulus input and their spatial arrangement across the cortical surface. The confluence of these observations  
31 is referred to as *functional organization*, the reproducible spatial arrangement of neurons within a cortical area  
32 according to their response properties. Functional organization is among the most ubiquitous of neuroscience  
33 findings, appearing in the topographic maps of the visual system [1], and in auditory [2], parietal [3], sensorimotor [4],  
34 and entorhinal areas [5, 6]. These organized structures anchor our understanding of cortical development, function,  
35 and dysfunction, yet it remains a mystery what processes govern their emergence, and what computational function  
36 they serve.

37 Any theory of functional organization must explain both neuronal response properties and the physical arrangement  
38 of neurons within a cortical area. Furthermore, a *unified* theory should account for the observed functional  
39 organization in multiple cortical areas. Prior computational models of the organization within single cortical areas  
40 have been developed [7, 8, 9, 10, 11, 12, 13, 14, 15, 16, 17, 18, 19, 20, 21, 22], but these approaches do not  
41 generalize to multiple cortical areas. Moreover, many of these models operate from a hand-crafted set of stimulus  
42 features, and thus cannot explain how neuronal response properties are learned from realistic sensory inputs.  
43 On the other hand, deep artificial neural networks (DANNs) trained with large quantities of naturalistic data are  
44 increasingly being used to model neuronal responses in regions responsible for vision, audition, and language  
45 processing [23, 24, 25, 26, 27, 28, 29, 30, 31]. However, standard DANNs impose no spatial arrangement among  
46 model units that differ in their stimulus tuning, and thus cannot explain the observed organization of neurons across  
47 the cortical surface.

48 Here, we introduce the Topographic Deep Artificial Neural Network (TDANN), a unified framework for predicting  
49 functional organization in sensory systems. The TDANN implements the hypothesis that neural systems are  
50 optimized to address two key goals: they must support ecologically-relevant behaviors by producing useful neural  
51 representations [32], and they must do so in a biophysically efficient manner, using as few resources as possible. A  
52 critical component of biophysical efficiency is the minimization of neuronal wiring length, which is theorized to result  
53 in the smooth topographic organization observed in many cortical areas [33, 19, 18]. The TDANN begins with a  
54 standard DANN and spatially augments it by embedding each layer's units in a two-dimensional simulated cortical  
55 sheet. The TDANN then optimizes a *composite objective function* with two components: a functional objective  
56 that drives the learning of useful representations, and a spatial constraint that encourages efficiency with smooth  
57 response patterns across the simulated cortical sheet. We test this framework in the primate ventral visual stream,  
58 a cortical system in which functional organization has been extensively documented.

59 The ventral stream is a hierarchical series of cortical areas that support visual recognition, beginning with primary  
60 visual cortex (V1) and ascending through intermediate areas (e.g., V4) to high-level regions: inferotemporal (IT)  
61 cortex in macaques and ventral temporal cortex (VTC) in humans. Well-known neuronal response properties in V1  
62 include tuning to edge orientation [1, 34, 35], spatial frequency [36], and color [37, 38]. These response properties  
63 are coupled with topographic signatures: orientation preferences form a smooth cortical map with pinwheel-like  
64 discontinuities [39, 40, 41, 42, 43]; spatial frequency tuning is organized in a quasi-periodic map with isolated  
65 low-frequency domains [42, 43, 44]; and color-preferring neurons cluster in punctate blobs [38] across the V1 surface.  
66 Higher-level regions such as primate IT [45, 46, 47, 48] and the analogous human VTC contain neurons with stronger  
67 responses for items of specific categories vs. others (e.g., faces vs non-faces), a property known as *category*  
68 *selectivity*. A core characteristic of functional organization in IT [48, 49] and VTC [50, 51, 52, 53, 54, 55, 56] is that  
69 neurons selective for certain ecologically-relevant categories – including faces, places, limbs, and visual wordforms  
70 – cluster into spatial patches, with characteristic patch sizes, counts, and relative inter-patch distances.

71 We find that the TDANN reproduces the functional organization of the ventral stream, including smooth orientation  
72 maps with pinwheels in an earlier model layer, and category-selective patches in a later layer that match the number,  
73 size, and relative geometry of patches in human VTC. To understand the principles underlying the emergence of the  
74 ventral stream's functional organization, we then test which specific functional and spatial constraints of the TDANN  
75 are critical to the TDANN's success by insantiating alternative models and measuring their capacity to predict neural  
76 data. We find that the specific combination of task and spatial objectives that best matches the functional organization  
77 of the ventral stream also makes learned representations more brain-like by constraining their intrinsic dimensionality.  
78 The TDANN learns these representations while minimizing the network's inter-layer wiring length, suggesting that  
79 brain-like functional organization effectively balances performance with metabolic costs.

80 Finally, because the the TDANN accurately predicts the functional organization of the ventral stream, it provides  
81 an exciting new platform for simulating experiments that are challenging to implement empirically. As a proof of  
82 principle, we perform *in silico* experiments simulating the effect of cortical microstimulation devices that vary in their

<sup>83</sup> spatial precision and cortical coverage. Taken together, our results show that the TDANN serves both as a unified  
<sup>84</sup> explanation for the functional organization of the visual system and as a platform to fuel discovery in neuroscience.

## 85 Results

### 86 Instantiating models that balance task performance with spatial smoothness

87 Building on optimization-based approaches in computational neuroscience [57, 58], we seek a model architecture  
88 and objective function that generate a neural network which matches the neuronal responses and topography of the  
89 primate ventral visual stream.

90 Because standard DANNs have no within-area spatial structure beyond retinotopy, we must augment their  
91 architecture to model spatial topography. Specifically, we take the ResNet-18 architecture [59], a DANN that achieves  
92 strong object recognition performance and accurate prediction of neuronal responses throughout the ventral visual  
93 stream [30], and augment it by embedding the units of each convolutional layer into a two-dimensional simulated  
94 cortical sheet (Figure 1a). Given that neurons in visual cortex are organized retinotopically at birth [60], we assign  
95 model unit positions retinotopically, such that units responding to similar regions of the input images are nearby in  
96 the simulated cortical sheet. Then, prior to training, unit positions are locally shuffled to circumvent limitations of  
97 weight-shared convolution (see Methods). The size of the simulated cortical sheet in each layer is anchored by  
98 estimates of cortical surface area in the human ventral visual stream (Figure 1a). We refer to the resulting model as  
99 the *Topographic DANN (TDANN)*.

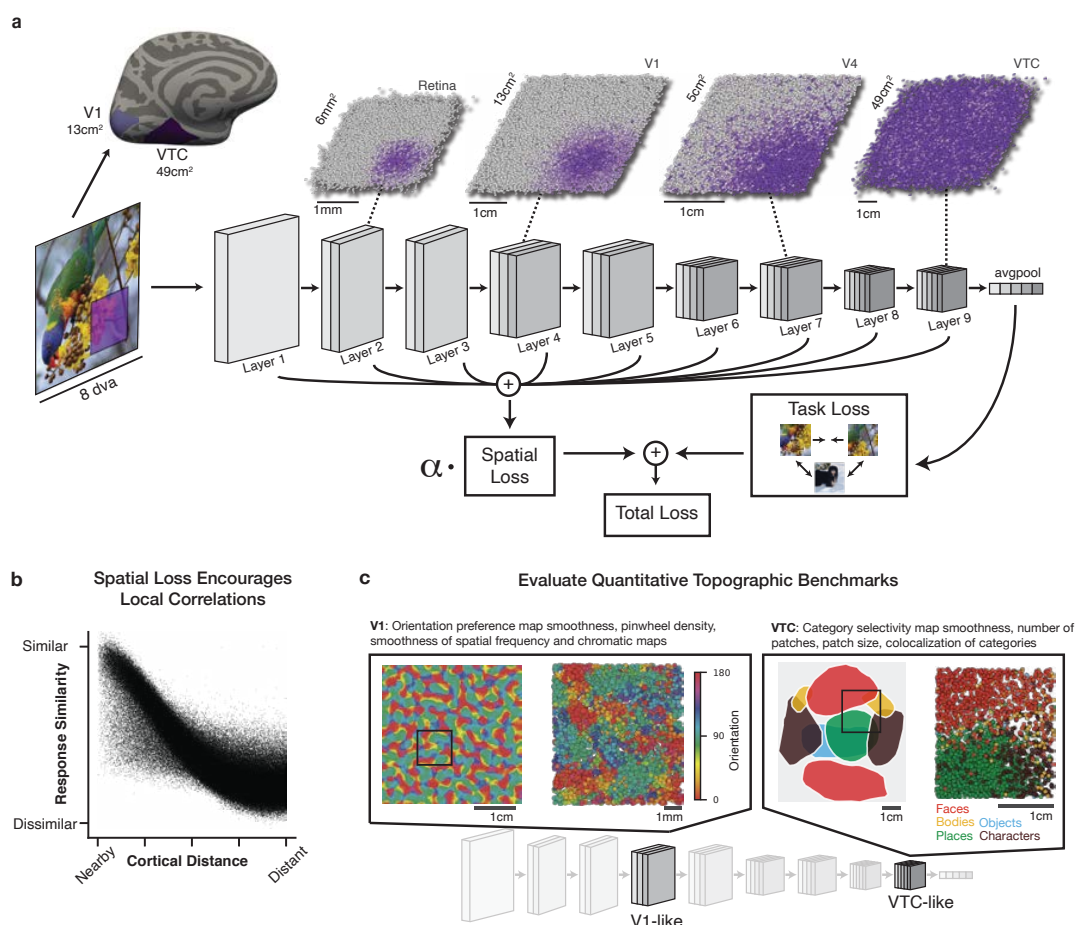


**Figure 1. Constructing a unified model of the functional and spatial constraints of ventral visual cortex.** (a) TDANNs are a family of deep artificial neural networks whose units are assigned positions in a two-dimensional simulated cortical sheet in each layer. Position assignments are retinotopic, such that location in the cortical sheet corresponds to position in the visual field. Each individual dot is a single model unit. The degree of overlap between a unit's spatial receptive field (RF) and the purple square marked on the input image is indicated by the shade of purple; RFs from gray units do not overlap the marked region at all. The TDANN is trained to minimize the sum of a task loss and a spatial loss (SL).  $\alpha$  is a free parameter controlling the relative weight of the SL. (b) The SL encourages nearby units to develop strong response correlations. Plotted: pairwise similarity of unit responses as a function of pairwise cortical distance in the final layer of a TDANN model; each dot represents one pair of units. (c) The TDANN is evaluated on a battery of quantitative benchmarks that measure its correspondence to topographic features throughout the ventral visual stream. Left: orientation preference map in the V1-like TDANN layer (see Figure 2 for details). Right: category selectivity map in the VTC-like layer (see Figure 3 for details).

100 Having selected the architecture, our goal is to discover the objective whose optimization yields an accurate model  
101 of both response properties and their topographic arrangement. The core of the TDANN approach is a composite  
102 objective that is a weighted sum of two components: a task objective encouraging the learning of behaviorally-useful  
103 functional representations, and a spatial objective driving the emergence of topographic properties. Following recent  
104 progress in training neural networks without explicit category labels [61, 62], we use an unsupervised algorithm that  
105 performs *contrastive self-supervision*, SimCLR [63], as the task objective. For the spatial loss (SL), we introduce an  
106 objective that encourages nearby pairs of units to have more correlated responses than distant pairs of units (Figure  
107 1b, see Methods). The SL is computed separately in each convolutional layer, then summed across layers for each  
108 batch of training data:

$$\text{TDANN Loss} = L_{\text{task}} + \sum_{k \in \text{layers}} \alpha_k \text{SL}_k \quad (1)$$

109 where  $\alpha_k$  is the weight of the spatial loss in the  $k$ th layer, set to  $\alpha_k = 0.25$  for all layers. The TDANN architecture is  
110 trained to optimize this objective using conventional back-propagation with stochastic gradient descent.

111 Training the TDANN on ImageNet [64] resulted in successful minimization of both task and spatial losses  
112 (Supplementary Figure S1). We tested if adding the spatial loss interferes with visual representation learning by  
113 measuring the model's object categorization performance with a linear readout. Categorization accuracy was slightly  
114 but significantly lower for the TDANN (median across random initialization seeds = 43.9%) than "Task Only" models  
115 with no spatial loss ( $\alpha = 0$ , median = 48.5%; Mann-Whitney  $U = 25, p = .008$ ). Despite the modest decrease in  
116 categorization performance, adding the spatial loss term had the intended effect: in each layer, the correlation  
117 between units' responses increased with spatial proximity (Supplementary Figure S1c,d). To determine if this  
118 learned correlation structure corresponds to brain-like topographic maps, we constructed a battery of quantitative  
119 benchmarks comparing model predictions with neural data in primary visual cortex (V1) and ventral temporal cortex  
120 (VTC), (Figure 1c). To compare against these benchmarks, we needed to identify the TDANN layers that would be  
121 our models of V1 and VTC. As in prior work [28, 25], we find that earlier model layers best predict V1 responses and  
122 later layers best predict responses in higher visual cortex (Supplementary Figure S2). Accordingly, we designate the  
123 fourth and ninth convolutional layers as the "V1-like" and "VTC-like" layers, respectively.

## 124 The TDANN predicts the functional organization of primary visual cortex

125 Neurons in primate V1 are organized into maps of preferred stimulus orientation, spatial frequency, and color  
126 [38, 43, 65]. Because high-resolution data at the scale necessary to visualize these maps is not available for  
127 human V1, we compare the TDANN to macaque V1 data using scale-invariant metrics. We tested if the V1-like  
128 TDANN layer captures the functional organization of macaque V1 with three kinds of quantitative benchmarks. First,  
129 we evaluate functional correspondence by asking if model units in the TDANN V1-like layer have similar preferred  
130 orientations and orientation tuning strengths as neurons in macaque V1. Second, we assay the structure of cortical  
131 maps by measuring pairwise similarity of tuning for orientations, spatial frequencies, and colors as a function of  
132 cortical distance. Third, we measure the density of pinwheel-like discontinuities in the orientation preference map,  
133 a hallmark of V1 functional organization in many species [41, 66]. In addition to the TDANN, we also evaluate four  
134 control models on these benchmarks: the *Unoptimized* TDANN, in which model weights and unit positions are left  
135 randomly initialized, the *Task Only* variant in which  $\alpha = 0$ , and two kinds of self-organizing maps (SOMs), which have  
136 been proposed as models of V1 functional organization [11, 10]. We refer to the traditional SOM in which feature  
137 dimensions are manually predetermined (as in Swindale and Bauer [11]), as the Hand-Crafted SOM, and a novel  
138 SOM that organizes the output of an AlexNet V1-like layer (inspired by Doshi and Konkle [13], Zhang et al. [12]) as  
139 the DNN-SOM.

140 **The TDANN matches orientation tuning in V1** We measured orientation tuning strength by presenting a set of  
141 oriented sine grating images to the model (Figure 2a), computing a tuning curve for each unit, and calculating  
142 the circular variance (CV; lower values for sharper tuning) of each tuning curve. Setting a selectivity threshold of CV  
143  $< 0.6$ , we find that the TDANN V1-like layer has a significantly greater proportion of selective units (range across  
144 model seeds: [20%, 31%]) than Unoptimized models ([1%, 3%]; Mann-Whitney  $U = 25; p = .008$ , Figure 2b), but  
145 fewer than Task Only models ([35%, 50%];  $U = 25; p = .008$ ) or macaque V1 (45%; Supplementary Figure S3c). In  
146 contrast, neither the Hand-Crafted SOM nor the DNN-SOM exhibited any units with sharp orientation tuning. We  
147 also find that TDANN and Task Only models (but not SOMs or Unoptimized models) show an over-representation of  
148 cardinal orientations (0 and 90 degrees) as in macaque V1 [35] (Supplementary Figure S3b, see also Henderson  
149 and Serences [67]).

150 **The TDANN predicts the arrangement of orientation-selective V1 neurons** To evaluate whether the TDANN V1-like  
151 layer captures the topographic properties of macaque V1, we consider the spatial distribution of orientation-selective  
152 units – the orientation preference map (OPM) – and find a smooth progression of preferred orientations that

resembles macaque V1 (Figure 2c, d). Following prior work [68, 69, 70], we quantify this structure by measuring the absolute pairwise difference in preferred orientation as a function of cortical distance. In both the TDANN and macaque V1 (data from Nauhaus et al. [43]), we find that nearby units have smaller differences in orientation preference than distant pairs (Figure 2e). In contrast, orientation preference similarity does not vary with cortical distance in Task Only or Unoptimized models, and both the Hand-Crafted and DNN-SOMs exhibit OPMs with abnormally high orientation tuning similarity (Figure 2e, Supplementary Figure S3). We summarize these profiles by computing a *smoothness score* that measures the increase in tuning similarity for nearby unit pairs compared to distant unit pairs. Smoothness of TDANN OPMs ([min, max] across random initialization: [.64, .83]) was consistent with macaque V1 (.68); however, OPMs in the Hand-Crafted SOM ([.92, .92]) and DNN-SOMs ([.81, .86]) were smoother than in macaque V1. In turn, macaque V1 OPMs were smoother than Unoptimized ([.03, .04]) and Task Only ([.28, .39]) models. Jointly comparing each model to macaque V1 orientation tuning strength and OPM smoothness highlights that the TDANN is the only model class that satisfies both criteria (Figure 2j).

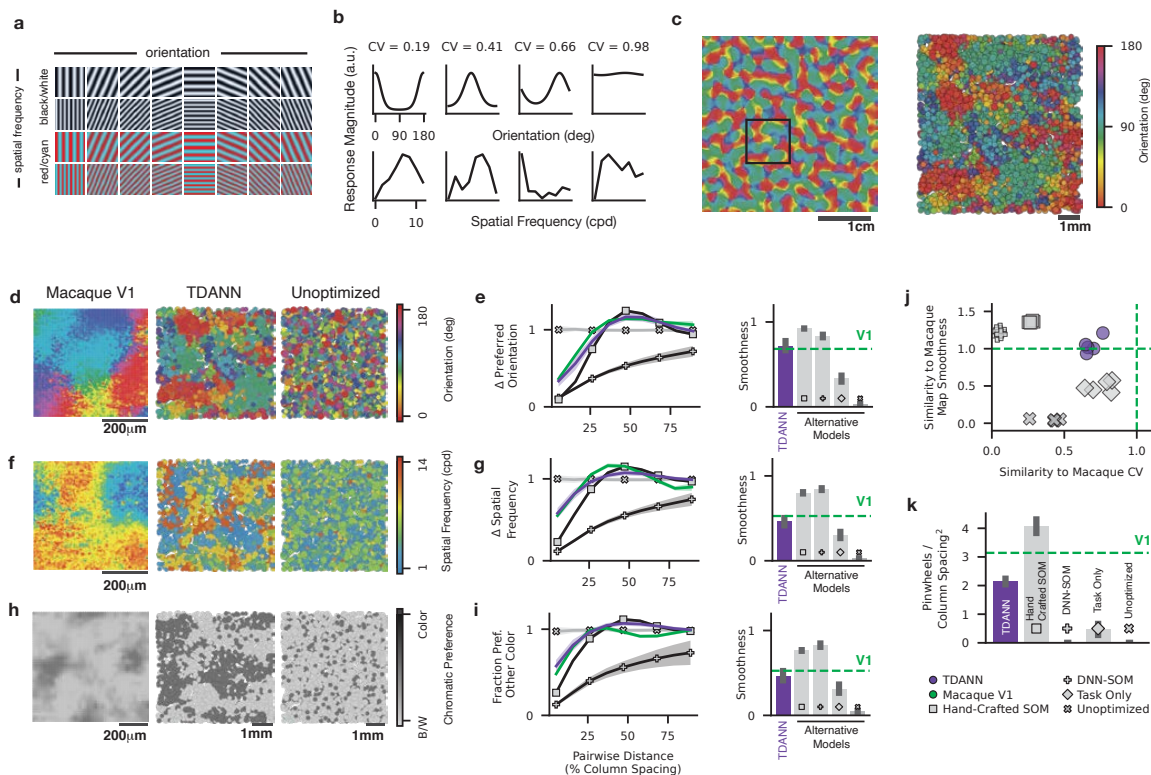


**Figure 2. The TDANN reproduces V1-like topography.** (a) Example sine grating stimuli used to assess tuning for orientation, spatial frequency, and color. (b) Orientation tuning curves (top) and spatial frequency tuning curves (bottom) for four example units in the V1-like layer. (c) Smoothed orientation preference map (OPM) in the V1-like layer of the TDANN. Box corresponds to inset at right, where individual model units are labeled by their preferred orientation. Results for additional model seeds shown in Supplementary Figure S10. (d) OPMs for Macaque V1 (data from Nauhaus et al. [43]), TDANN, and an Unoptimized control model. (e) Left: Pairwise difference in preferred orientations as a function of pairwise cortical distance, normalized to the chance level expected by random sampling of pairs. Right: Map smoothness for OPMs in macaque V1 (dashed green line, data from Nauhaus et al. [43]) and four candidate models: the TDANN (purple), the Hand-Crafted self-organizing map (SOM, squares), deep neural network SOM (DNN-SOM, plus signs), and Task Only (diamonds) trained without the spatial term of the loss function. Error bar: 95% CI across random model seeds and sampling of cortical neighborhoods. (f) Spatial frequency preference, shown for the same region of the TDANN V1-like layer and macaque V1 as in panel (d). (g) Change in preferred spatial frequency as a function of cortical distance, normalized to chance, for macaque V1 and each model type. (h) Preference for chromatic stimuli for the same region of the TDANN V1-like layer. Dark-colored dots: stronger responses to chromatic than achromatic gratings. Macaque data: reconstruction of cytochrome oxidase staining data from Livingstone and Hubel [38]. (i) Fraction of units differing in their chromatic preference as a function of cortical distance, normalized to chance. (j) Similarity of models to the distribution of orientation tuning strengths in macaque V1 (data from Ringach et al. [34]) on the x-axis, and similarity to the smoothness of macaque OPMs (data from Nauhaus et al. [43]) on the y-axis. Multiple markers of the same type indicate different random initial seeds for each model. A value of 1.0 (dashed green) indicates perfect correspondence. (k) Density of pinwheels detected in TDANNs, Hand-Crafted SOMs, Task Only models, and Unoptimized models. Error bars: CI across random model seeds. Green: putative macaque V1 pinwheel density.

165 As a more stringent test of OPM structure, we counted the number of periodic pinwheel-like discontinuities in the  
166 OPM [41] and compared to the expected value of  $\sim 3.1$  pinwheels /  $mm^2$  in macaque V1 [66]. Multiple pinwheels are  
167 apparent in both the TDANN and the Hand-Crafted SOM (Figure 2k). To facilitate quantitative comparison across  
168 models, we compute pinwheel *density* – the number of pinwheels normalized by the average spacing between  
169 "columns", i.e. clusters of units preferring the same orientation. We find that the TDANN has lower pinwheel density  
170 (range across seeds = [2.0, 2.3] pinwheels / column spacing<sup>2</sup>) than macaque V1, but significantly higher than either  
171 the Task Only ([0.2, 0.8]; Mann-Whitney  $U = 25, p = .008$ ) or Unoptimized models (0 pinwheels; Figure 2k). The  
172 Hand-Crafted SOM has higher pinwheel density ([3.7, 4.5]) than the TDANN, but the DNN-SOM has no detectable  
173 pinwheels. Although the TDANN has pinwheel density approaching that of macaque V1, we note that the orientation  
174 column spacing in the TDANN ( $\sim 3.5$ mm width) does not match macaque V1 ( $\sim 1$ mm). This mismatch, caused  
175 in part by our commitment of the TDANN as a model of human visual cortex and not macaque visual cortex, can  
176 also be overcome by increasing the number of units in the network at the expense of increased computational cost  
177 (Supplementary Figure S5).

178 **The TDANN predicts maps of spatial frequency and color preference in V1** While OPMs are the best-studied feature  
179 of V1 functional organization, the cortical sheet simultaneously accommodates organized maps of spatial frequency  
180 [43] and chromatic tuning [71, 38]. An accurate model of V1 should also predict these aspects of V1 functional  
181 organization. We compared spatial frequency preference maps in macaque V1 (data from [43]) and in the TDANN  
182 V1-like layer and found a smooth progression of preferred spatial frequency in both (Figure 2f). Quantifying the  
183 difference in spatial frequency tuning as a function of cortical distance indicates that the TDANN map ([min, max]  
184 of smoothness across random initializations = [.38, .54]) is as smooth as the map in macaque V1 (0.53; Figure 2g),  
185 whereas maps from Task Only ([.23, .36]) and Unoptimized models ([.02, .03]) are far less smooth than macaque V1,  
186 and both the Hand-Crafted SOM ([.79, .81]) and the DNN-SOM ([.83, .86]) are again far smoother than the neural  
187 data. We observe similar results for maps of chromatic preference (Figure 2h, i), where comparisons are made  
188 to imaging of cytochrome oxidase (CO) uptake that is prevalent in color-tuned neurons (data from Livingstone and  
189 Hubel [38]). In the TDANN chromatic map, the fraction of units with opposite color-tuning increases with cortical  
190 distance, again exhibiting comparable smoothness to macaque V1 (TDANN smoothness: [.38, .54], macaque: .53).  
191 Together, our analyses demonstrate that the TDANN predicts the multifaceted functional organization of macaque  
192 V1, providing a stronger match to neural data than existing models such as the standard Hand-Crafted SOM.

### 193 **The TDANN reproduces the functional organization of higher visual cortex**

194 Because benchmarks measuring the topographic similarity between models and higher visual cortex, i.e. primate  
195 inferior temporal (IT) and human ventral temporal cortex (VTC), are still underdeveloped, we introduce five  
196 quantitative benchmarks that compare both responses and topography. Response properties are compared by  
197 measuring the similarity of population category selectivity patterns with representational similarity analysis (RSA;  
198 Kriegeskorte et al. [72]), as in Margalit et al. [73], Haxby et al. [74]). Topographic properties are then compared  
199 against four complementary benchmarks: 1) the smoothness of category selectivity maps, 2) the number of category  
200 selective patches, 3) the area occupied by those patches, and 4) the spatial overlap of units selective for different  
201 categories. We compute these metrics for the TDANN's VTC-like layer and for VTC data from eight human subjects  
202 in the Natural Scenes Dataset (NSD) [75] (Supplementary Figure S6). We also evaluate two alternative models of  
203 VTC topography: an SOM trained on the outputs of a categorization-pretrained AlexNet (DNN-SOM, cf Doshi and  
204 Konkle [13], Zhang et al. [12]) and a variant of the Interactive Topographic Network (ITN) that is trained on the same  
205 dataset (ImageNet) we used (Blauch et al. [20]: Supplementary Figure S19C). Human subjects and models were all  
206 presented a common set of 1,440 object category images [76] composed of five categories: faces, bodies, written  
207 characters, places, and objects (cars and instruments). Selectivity was computed as the  $t$ -value for each category,  
208 for each human voxel and model unit.

209 **The TDANN predicts patterns of category selectivity** We characterize neuronal responses in VTC by computing a  
210 representational similarity matrix (RSM): the similarity between pairs of distributed selectivity patterns to each of the  
211 five object categories. The average RSM from human VTC indicates high similarity between patterns of selectivity  
212 for faces and bodies, and low similarity between selectivity for faces and places (Figure 3a). The alignment between  
213 any two RSMs is computed as Kendall's  $\tau$ . RSMs from different subjects and hemispheres were very similar, with  
214 the 95% CI of Kendall's  $\tau = [.72, .75]$ . We then compute RSMs for each model and compare against the human data,  
215 finding that some models provide a closer match to human VTC than others (ANOVA  $F(4, 331) = 630; p < 10^{-152}$ ).  
216 TDANN RSMs closely mirror those in human VTC ( $\tau = [.69, .73]$ ), significantly better than DNN-SOM ( $\tau = [.31, .35]$ ;  
217 post-hoc Tukey's HSD  $p < 10^{-13}$ ), ITN ( $\tau = [.46, .56]; p < 10^{-13}$ ), Task Only ( $\tau = [.65, .68]; p = .001$ ) and Unoptimized  
218 ( $\tau = [.11, .14]; p < 10^{-13}$ ) models (Figure 3b). The similarity between human and TDANN RSMs also depends  
219 strongly on the training data being naturalistic. Training on artificial stimuli such as white noise and sine gratings  
220 yields RSMs that significantly deviate from the human data (Supplementary Figure S9b).

221 **The TDANN predicts category-selectivity maps** To compare models against topographic benchmarks, we generate  
 222 selectivity maps for each of the five object categories (Figure 3c), then quantify their structure by measuring the  
 223 pairwise difference in selectivity as a function of pairwise cortical distance (Figure 3d). We find that for all categories,  
 224 the curve computed for TDANN is similar to human VTC, whereas the DNN-SOM and ITN are abiologically smooth,  
 225 and maps in the Unoptimized and Task Only models lack structure. We summarize category selectivity map structure  
 226 with the same smoothness metric used in V1 (Figure 3e), and find that TDANN maps were as smooth as those in  
 227 human VTC (permutation test:  $p = .30$ ). In contrast, VTC maps were significantly smoother than Task Only or  
 228 Unoptimized models ( $p < .001$ ) and less smooth than the DNN-SOM ( $p < .001$ ). ITN category selectivity maps were  
 229 smoother on average than VTC, but not significantly so ( $p = .10$ ).

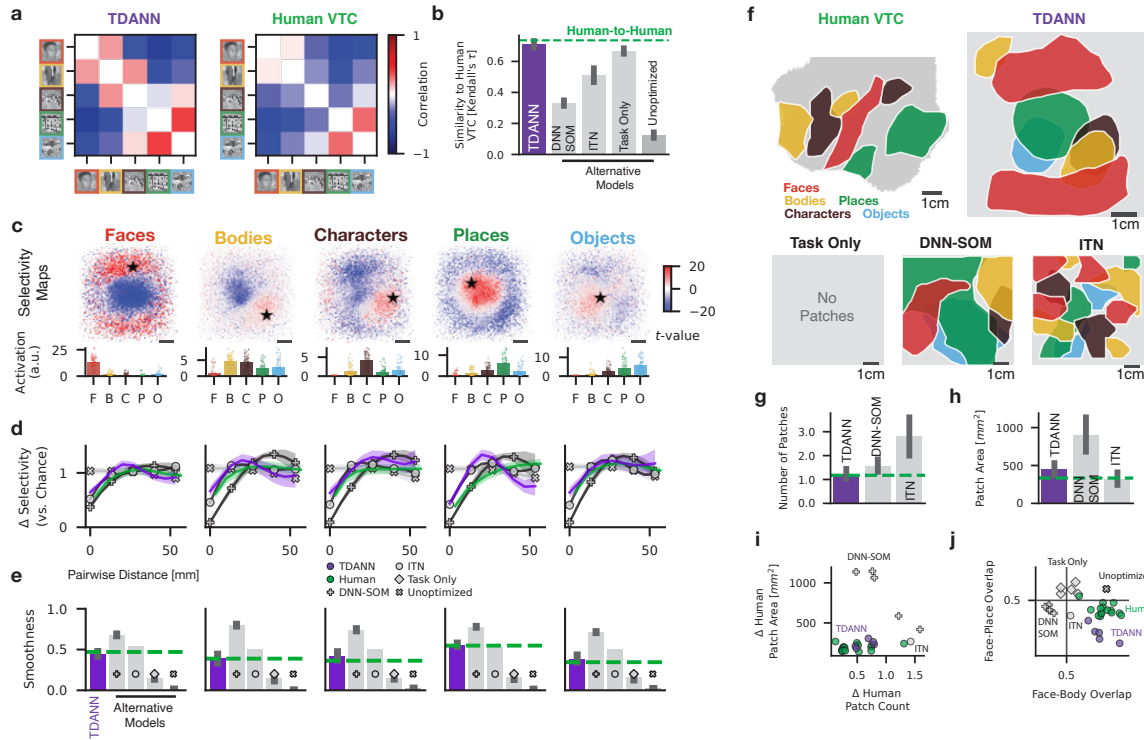


**Figure 3. The TDANN predicts the functional organization of higher visual cortex.** (a) Representational similarity matrices (RSMs) for the TDANN and human VTC, computed across selectivity maps of the five object categories. Diagonal is blank to indicate trivially perfect correlation. (b) Functional similarity between the TDANN, human VTC, and alternative models, measured as the similarity of RSMs. Green: mean of pairwise human-to-human similarity values. (c) Selectivity ( $t$ -value), for each category plotted on the simulated cortical sheet of the VTC-like layer in an example TDANN. Black star: unit whose responses to images in each of the five categories are plotted directly below (individual dots: single images, bar height: mean across images). Scale bar: 1cm. (d) Difference in pairwise selectivity as a function of pairwise cortical distance for units in each of five candidate model types: the TDANN (purple), deep neural network self-organizing map (DNN-SOM; plus markers), interactive topographic network ("ITN", Blauch et al. [20]; circles), Unoptimized ("x" markers), and Task Only (diamond markers). Curves are normalized to the chance level obtained by random sampling of unit pairs. Green: Human data averaged over the eight subjects in the NSD data. Shaded regions: 95% confidence interval across different subsets of units from models trained with different random initial seeds. (e) Smoothness of selectivity maps for each category and each candidate model. Dashed green: mean of human data. (f) Category-selective patches for an example hemisphere in human ventral temporal cortex (VTC), TDANN, a Task Only model (no patches detected), a DNN-SOM, and a reproduction of the "ITN" simulated cortical sheet from [20]. Object categories are indexed by color as in (a) and (c). Examples from different initial random seeds are shown in Supplementary Figure S10. (g) Number of category-selective patches (averaged across categories) for the TDANN, DNN-SOM, and ITN. Dashed green: average of human data. ANOVA for difference in patch count:  $F(5, 179) = 32.7, p < 10^{-22}$ . Post-hoc Tukey's tests: significant difference between VTC and ITN ( $p = 1.2 \times 10^{-5}$ ). (h) Average surface area of category-selective patches. Same plotting conventions as in (f). ANOVA for difference in patch area:  $F(5, 187) = 15.4, p < 10^{-11}$ . Post-hoc Tukey's tests: significant difference between VTC and DNN-SOM ( $p < 10^{-10}$ ). (i) Each human subject and model instance compared to the mean patch area (y-axis) and patch number (x-axis) in the human data. (j) Overlap between face-selectivity and body-selectivity vs. overlap between face-selectivity and place-selectivity, for each human hemisphere (green dots), each TDANN instance (purple dots), the ITN (gray dot), each DNN-SOM (gray plus signs), and Task Only models (gray diamonds).

230 For the remaining topographic benchmarks, we follow the literature by thresholding selectivity maps to find



231 strongly-selective units (Supplementary Figure S6a-d). Clusters of selective units are identifiable in human VTC,  
232 TDANN, the SOM and ITN models, but not in Task Only or Unoptimized models. We use a data-driven approach  
233 to automatically identify large contiguous clusters of selective units as "patches" (Figure 3f). We find similar sets  
234 of patches in VTC and the TDANN: both contain a small number of patches selective for each category (except for  
235 object-selective patches, which are not found in VTC), and the patches are similar in size. Quantitative comparison  
236 supports the similarity of human VTC and TDANN: there is no significant difference in patch count ( $p = 0.99$ , Figure  
237 3g) or patch area ( $p = 0.67$ ; Figure 3h). In contrast, we find that the ITN has more than twice as many patches as  
238 VTC ( $p = 1.2 \times 10^{-5}$ ), although the patches are as large on average as those in VTC ( $p = 0.99$ ). The DNN-SOM  
239 fails to match VTC in the other extreme: while the number of patches in the DNN-SOM is similar to that in VTC  
240 ( $p = 0.15$ ), the patches are too large ( $p < 10^{-10}$ ). Joint comparison of models and humans on both patch count and  
241 size (Figure 3i) highlights the stronger correspondence between TDANN and human VTC than alternative models.

242 An important hallmark of the functional organization of higher visual cortex is the reproducible spatial arrangement  
243 of units selective for different categories. A prominent example is the close proximity of face-selective and  
244 body-selective regions [49, 77] and the separation between face- and place-selective regions. A measure of proximity  
245 between face- and body-selective regions was previously introduced in Lee et al. [78]. Here we measured the  
246 co-occurrence of face-selective and body-selective units (and face-selective and place-selective units) in human  
247 VTC with an overlap score that ranges between 1 (face-selectivity perfectly predicts body-selectivity) to 0.5 (no  
248 relationship), to 0 (face- and body-selectivity perfectly anti-correlated). As expected, Face-Body overlap scores  
249 are high in human VTC (95% CI across subjects and hemispheres: [.66, .72]), whereas Face-Place overlap  
250 was significantly lower (95% CI: [.40, .45], Wilcoxon signed-rank test against one-sided alternative  $W = 136; p =$   
251  $1.5 \times 10^{-5}$ ; Figure 3j). The same pattern is apparent in the TDANN: Face-Body Overlap (.63, .71) is significantly  
252 higher than Face-Place Overlap (.14, .26;  $W = 15; p = .03$ ). In the ITN, the Face-Body overlap score was lower  
253 than in human VTC (.52), but still higher than the Face-Place overlap score (.36). Neither the the DNN-SOM nor the  
254 Task Only models had higher Face-Body overlap than Face-Place overlap (Figure 3j;  $ps > 0.5$ ).

255 To further gain intuition for the tuning profiles of model units, we synthesized images that optimally drive each region  
256 of the VTC-like layer. We find that the VTC-like layer smoothly maps object feature space onto the two-dimensional  
257 simulated cortical sheet; e.g., face-patches are optimally driven by stimuli with apparent eyes (Supplementary Figure  
258 S7). We also tested how the nature of the training dataset affects the accuracy of topographic maps in the TDANN  
259 (see Lee et al. [78], Figure 7 for a similar analysis). We find that training the TDANN on natural images (either  
260 ImageNet [64] or Ecoset [79]) produces accurate V1-like and VTC-like maps, whereas training on noise or simpler  
261 hand-crafted stimuli fails to provide a unified account of ventral stream topography (Supplementary Figure S9).

262 Together, these results demonstrate that TDANN is the only model to exhibit spatially structured category selectivity  
263 that is consistent with a large battery of benchmarks comparing models to human VTC.

## 264 Multiple signatures of functional organization emerge at the same spatial constraint strength

265 The TDANN optimization framework requires the selection of a single free parameter,  $\alpha$ , the weight of the spatial loss  
266 in the training objective. When  $\alpha = 0$  ("Task Only"), spatial information is ignored during training, whereas setting  $\alpha$   
267 too high may encourage pathologically strong correlations that interfere with representation learning. In the results  
268 above,  $\alpha$  is set to 0.25. Here, we validate this choice by demonstrating that many benchmarks of neural similarity  
269 are simultaneously satisfied by low-to-intermediate values of  $\alpha$ .

270 Comparison of OPMs in the V1-like layer and category-selectivity maps in the VTC-like layer (Figure 4a) in models  
271 trained at 7 different levels of  $\alpha$  shows that functional organization is absent when  $\alpha = 0$ , structured at intermediate  
272 values of  $\alpha$ , and deteriorates at the highest values of  $\alpha$ . We quantify the dependence of functional organization  
273 on  $\alpha$  with three kinds of benchmarks: functional similarity (Figure 4b), map smoothness (Figure 4c), and presence  
274 of topographic phenomena (i.e. pinwheels and patches; Figure 4d). First considering functional similarity, we find  
275 that the fraction of V1-like layer units that are orientation selective is closest to macaque V1 when  $\alpha$  is low, and  
276 representational similarity between the VTC-like layer and human VTC is maximized at  $\alpha = 0.25$  (Figure 4b). The  
277 smoothness of topographic maps is most brain-like at  $\alpha = 0.1$  for OPMs in the V1-like layer and at  $\alpha = 0.25$  for  
278 category-selectivity maps in the VTC-like layer (Figure 4c). Finally, we find that the density of pinwheels in the  
279 V1-like layer and category-selectivity maps in the VTC-like layer are most similar to measurements in macaque V1  
280 and human VTC, respectively, at  $\alpha = 0.25$  (Figure 4d).

281 A specific range of  $\alpha$  values ( $0.1 \leq \alpha \leq 0.25$ ) thus produces experimentally-observed outcomes across a variety of  
282 independent functional and topographic benchmarks in multiple brain areas, suggesting that the  $\alpha$  parameter may  
283 provide insights into biophysical mechanisms underlying the emergence of functional organization.

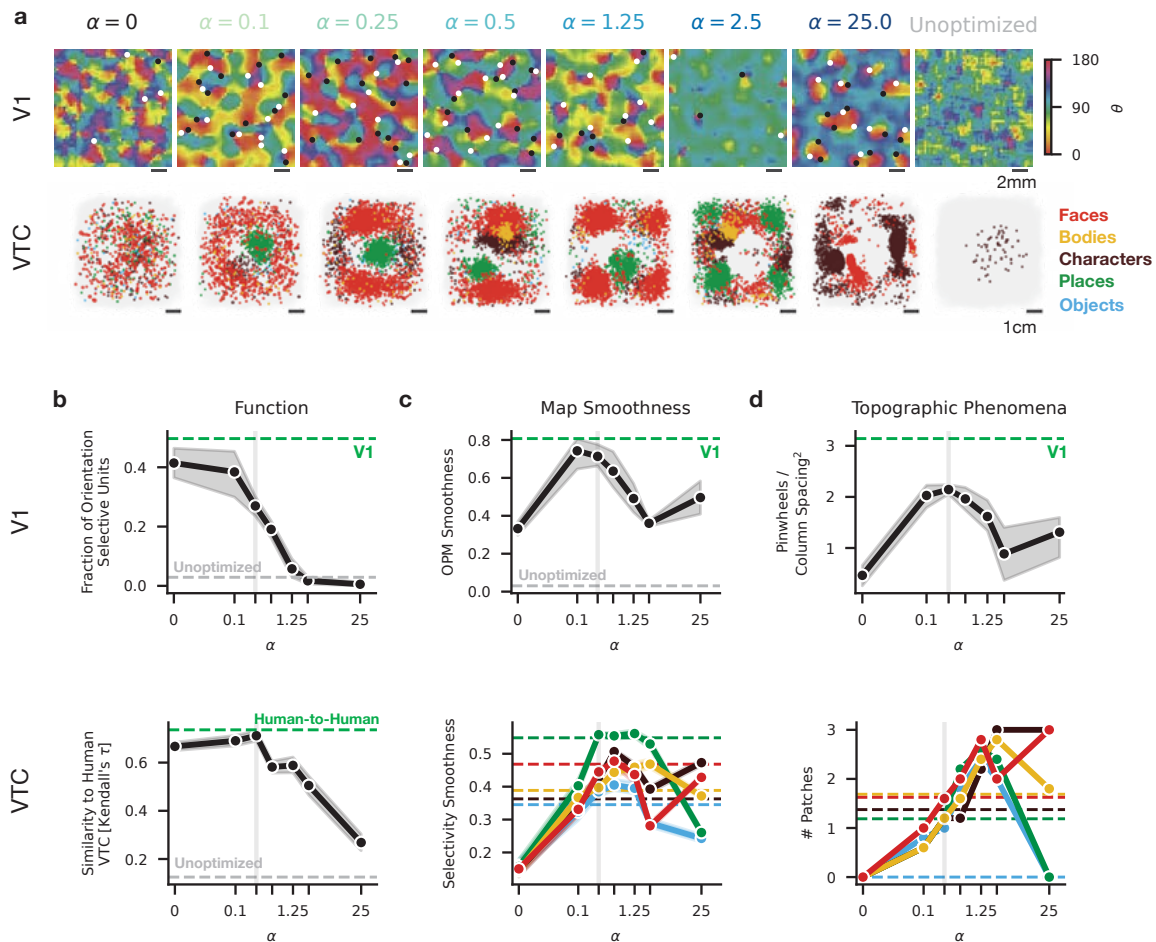


**Figure 4. Convergence of multiple benchmarks indicates a balancing between functional and spatial constraints. (a)** Topographic maps in the V1-like (top row) and VTC-like layer (bottom row) of TDANN models trained at different levels of the spatial weight  $\alpha$ . Top: Orientation map structure and pinwheels become apparent at  $\alpha > 0.1$  and persist until  $\alpha = 1.25$ . Dots: estimated pinwheel locations; black: clockwise, white: counterclockwise. Bottom: Category selectivity maps, with selective units ( $t > 12$ ) colored according to their preferred category. **(b)** Functional correspondence to neural data as a function of  $\alpha$ . Top: Fraction of units strongly orientation selective (circular variance  $\leq 0.6$ ) in the V1-like layer. Dashed green: value measured in macaque V1 (from Ringach et al. [34]). Dashed gray: mean value for Unoptimized models. Shaded regions: 95% CI across multiple initial random seeds. Bottom: Representational similarity between the VTC-like layer and human VTC (as in Figure 3). Error region indicates 95% CI across model seeds and human hemispheres. In both plots, the vertical line at  $\alpha = 0.25$  marks the default value used in prior figures. **(c)** Topographic map smoothness as a function of  $\alpha$ . Top: OPM smoothness in the V1-like layer. Dashed green: value in macaque V1. Dashed gray: smoothness in an Unoptimized model. Bottom: Category selectivity map smoothness in the VTC-like layer. Dashed lines indicate means across human subjects and hemispheres from the NSD data; one line per category. **(d)** Density of topographic phenomena of interest as a function of  $\alpha$ . Top: Pinwheel density in OPMs from the V1-like layer, as a function of  $\alpha$ . Bottom: Number of category selective patches for each category in the VTC-like layer, as a function of  $\alpha$ . Human data in dashed lines.

## 284 Two key factors underlying functional organization: self-supervised learning and a scalable spatial 285 constraint

286 Having established that specific TDANN models accurately predict the functional organization of the ventral visual  
287 stream, we consider what key factors enable the emergence of this functional organization. We reasoned that if  
288 some combinations of optimization objectives yield brain-like functional organization and others do not, it will shed  
289 light on the constraints underlying the observed functional organization. Thus, we train models with alternative task  
290 and spatial objectives, then apply our benchmarks to evaluate which models are most consistent with empirical data.

291 For the “task component” of its loss function, the TDANN uses contrastive self-supervision [61, 63], a framework for  
292 learning representations that transfer easily to many downstream tasks. These self-supervised algorithms have been  
293 shown to generalize to many downstream computer vision tasks despite being trained only on a large set of unlabeled

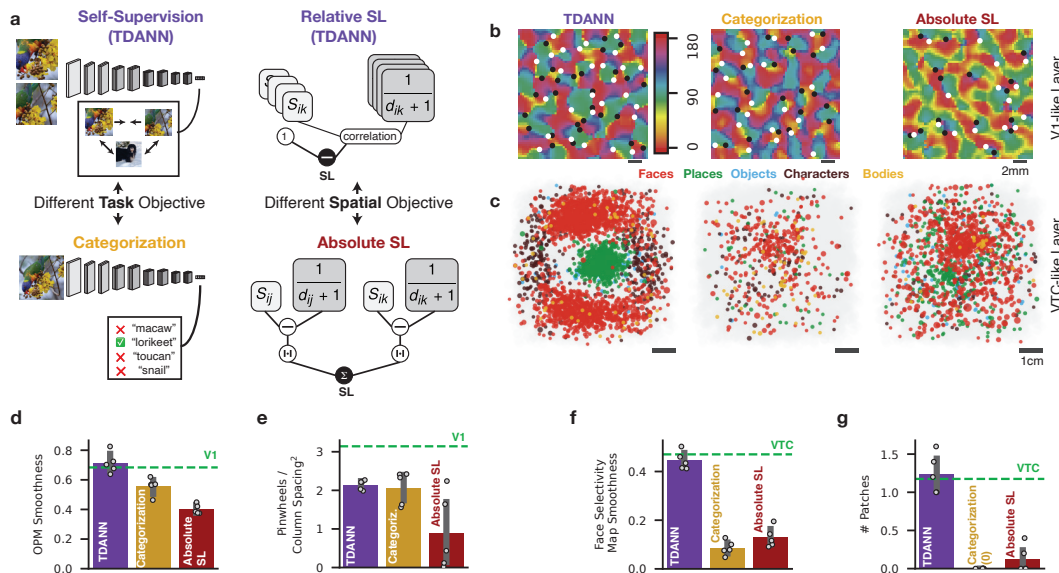


**Figure 5. Self-supervision and scalable spatial constraints under the emergence of functional organization.** In each panel, TDANN shown in purple, Categorization-trained in gold, Absolute SL in red, and ventral stream measurements in green. **(a)** Left: comparison of task objectives. The TDANN uses contrastive self-supervision (top) which encourages similarity between representations of different views of the same image while increasing distance between representations of views of other images. Categorization (bottom) compares predicted class probabilities to the human-labeled correct class. Right: comparison of spatial objectives.  $S_{ij}$ : response similarity of units  $i$  and  $j$ .  $d_{ij}$ : cortical distance between units  $i$  and  $j$ . TDANN uses the Relative SL (top), which correlates the population of response similarities and pairwise inverse distances. Prior work [78] used the Absolute SL (bottom), which directly subtracts inverse cortical distance from response similarity magnitude. **(b)** Smoothed orientation preference maps (OPMs) in the V1-like layer of the TDANN (left), a Categorization trained model (middle), and a model trained with the Absolute SL (right). Dots: detected pinwheels.  $\alpha = 0.25$  for models shown in each panel. **(c)** Category selective units in the VTC-like layer of the TDANN (left), a categorization trained model (middle) and a model trained with the absolute SL (right). **(d)** Right: Smoothness of OPMS in the V1-like layer of each model type. Green line: value computed macaque V1. **(e)** Density of detected pinwheels. Green: estimated value in macaque V1. **(f)** Right: Smoothness of face selectivity maps in the VTC-like layer of each model type. Green line: value from human VTC. **(g)** Average number of category-selective patches, in the VTC-like layer in each model. Green: average value in human VTC.

294 natural images [80]. However, most studies comparing neural networks to the brain have used a supervised object  
 295 categorization ([26, 25, 78]; Figure 5a-bottom left). Thus, we tested whether training with an object categorization  
 296 objective produces different functional organization than self-supervision, and if so, which is more similar to the  
 297 observed functional organization of the ventral visual stream.

298 We also investigate how the form of the spatial objective function affects emergent functional organization. The  
 299 spatial component of the TDANN loss function is generally intended to capture the constraints on unit-to-unit  
 300 correlations within cortical neighborhoods, but the specifics of its functional form embody conceptually distinct  
 301 mechanistic ideas about how a hypothetical cortical development circuit might measure functional correlations and  
 302 compare them to cortical distances. In prior work, Lee et al. [78] introduced a spatial loss function that subtracts  
 303 the inverse of pairwise cortical distances from the magnitude of pairwise response correlations (Figure 5a-bottom  
 304 right), such that nearby units develop similar responses. That loss function was developed to match empirical  
 305 measurements in macaque IT, but was not intended to generalize to other regions of the human ventral visual  
 306 stream. We refer to it as the Absolute Spatial Loss (or  $SL_{Abs}$ ), because minimizing it requires an absolute match  
 307 between response correlations and the inverse of cortical distances. While Lee et al. [78] found that training models  
 308 with  $SL_{Abs}$  produced clustering of category-selective units in a late model layer, we discovered a critical flaw when  
 309 training with  $SL_{Abs}$  in all model layers: in layers with shorter cortical distances,  $SL_{Abs}$  can only be minimized if  
 310 response correlations are pathologically high. The TDANN instead uses a more flexible spatial loss function that we  
 311 term the Relative Spatial Loss ( $SL_{Rel}$ ; Figure 5a-top right). This SL requires that inverse cortical distances will be  
 312 correlated with response similarity (see Methods for mathematical details).  $SL_{Rel}$  effectively enforces response  
 313 similarity between pairs of units that are *relatively* close together. Thus, the Relative SL allows the distance

314 over which local correlations extend to depend on the total size of the cortical area. Interestingly, we find that  
315 switching from  $SL_{Abs}$  to  $SL_{Rel}$  slightly increased the model's capacity for object categorization at all levels of  $\alpha$   
316 (Supplementary Figure S12). How do models trained for different objectives differ on topographic benchmarks?

317 We compare the TDANN (self-supervised and Relative SL) to categorization-trained models (differing only in task  
318 objective) and Absolute SL models (differing only in spatial objective) on our battery of topographic and functional  
319 benchmarks: (i) evaluating the smoothness of OPMs and face-selectivity maps in the V1-like and VTC-like layers,  
320 respectively, and (ii) counting the number of pinwheel-like discontinuities and category-selective patches in those  
321 layers, respectively. Categorization-trained models were slightly but significantly less smooth than the TDANN (mean  
322 smoothness = 0.56,  $U = 25, p = 0.008$ ), but with an equal density of pinwheels (2.07 pinwheels / column spacing<sup>2</sup>;  
323  $U = 10, p = 0.69$ ). Absolute SL models generally resemble those in the TDANN (Figure 5b), but with significantly  
324 lower smoothness (TDANN mean: 0.71, Absolute SL: 0.40;  $U = 25, p = 0.008$ ; Figure 5d) and slightly lower pinwheel  
325 density (TDANN: 2.14 pinwheels / column spacing<sup>2</sup>, Absolute SL: 0.89;  $U = 21, p = 0.09$ ; Figure 5e).

326 Strikingly, however, category-selectivity maps in the VTC-like layer were much less organized in the  
327 Categorization-trained models than in the self-supervised TDANNs. At the same spatial weight of  $\alpha = 0.25$ ,  
328 clear clusters of category-selective units are observed in the self-supervised but not the categorization-trained  
329 model (Figure 5c). The Absolute SL models also fail to form organized category-selectivity maps at this level  
330 of  $\alpha$ . Quantitative comparison reveals smoother category selectivity maps in the TDANN (mean smoothness of  
331 face-selectivity maps = 0.44) than in either categorization-trained models (0.09; Mann-Whitney  $U = 25, p = 0.008$ ;  
332 Figure 5f) or in Absolute SL models (0.13). The TDANN also has a significantly higher number of identified category  
333 selective patches (mean = 1.2) than either categorization-trained (mean = 0) or Absolute SL alternatives (mean  
334 = 0.08;  $U = 25, p = 0.008$ ; Figure 5g). Thus, the nature of the training objective strongly constrains the emergent  
335 functional organization, with self-supervised learning and relative spatial loss objectives producing the most brain-like  
336 functional organization.

### 337 **Spatial constraints make learned representations more brain-like by reducing intrinsic dimensionality**

338 A natural question is whether training for spatial objectives also has an effect on the *non-topographic* properties of  
339 learned representations. Because the TDANN allows the network's features to be influenced by the spatial constraint  
340 during training, we can directly address this question.

341 A powerful way to test if spatially-constrained models learn different features than standard DANNs is to measure  
342 how well model unit responses can predict neural responses to large set of naturalistic images in primate visual  
343 cortex [30, 28, 25, 81]. A popular approach to predicting neuronal firing rates is to fit the responses of individual  
344 neural units with a linear combination of many hundreds or thousands of model units. Consistent with prior work  
345 involving non-spatial models [61], we find that models trained with different objectives are largely indistinguishable  
346 in their ability to predict neural firing rates when using this standard linear-regression method for mapping model  
347 units to neural firing rates [25, 61, 29] (Figure 6a). The linear-regression mapping is thus insensitive to the dramatic  
348 differences between models trained with different objectives and spatial constraint magnitudes that are apparent in  
349 our analysis of functional organization. A possible explanation for this apparent discrepancy is that linear regression  
350 is too permissive of mapping: even if a model lacks individual units that resemble recorded neurons, a combination  
351 of units might still allow for accurate prediction of neural responses. We tested this prediction by performing a more  
352 stringent one-to-one mapping, in which individual VTC-like layer model units – not a linear mixture of units – are  
353 assigned to individual VTC voxels in a one-to-one fashion. Intriguingly, we found that this one-to-one assignment  
354 resulted in much stronger matches between TDANN model units and voxels recorded in the Natural Scenes Dataset  
355 (NSD) [75] than models trained with other objectives (i.e. categorization or Absolute SL, Figure 6b). This correlation  
356 peaks at  $\alpha = 0.25$ , the same value identified by topographic benchmarks (Figure 4), providing more evidence that  
357 the constraints driving brain-like functional organization also make learned representations more brain-like.

358 Many factors might contribute to the differences in representation between the TDANN and those of poorer-fitting  
359 models. Because the TDANN's spatial constraint encourages units to respond more similarly to one another, we  
360 hypothesized that the intrinsic dimensionality of the population might decrease as  $\alpha$  increases. Relatedly, recent  
361 work has demonstrated that spatially unconstrained DANN responses to natural images have substantially higher  
362 intrinsic dimension than real macaque and rodent V1, and that models with lower dimensionality better predict  
363 neural responses [82]. Thus, we tested whether decreased intrinsic dimensionality might explain why the TDANN  
364 representations are more brain-like than representations from other models. Consistent with our hypothesis, we  
365 find that the addition of the spatial constraint decreases intrinsic dimensionality in the VTC-like layer regardless of  
366 the training objective (Figure 6c; see Supplementary Figure S13a for eigenspectra in all layers). When  $\alpha = 0$ , all  
367 models have higher effective dimensionality (ED; Elmoznino and Bonner [83], Del Giudice [84]; see methods) than  
368 human VTC (mean across subjects = 16.7), although the dimensionality of the VTC-like layer in categorization-trained

369 models (76.8) is nearly three times higher than in the self-supervised models (TDANN and Absolute SL: 27.8). At  
 370 the spatial weight magnitude  $\alpha = 0.25$ , at which the TDANN best matches neural data, the TDANN's VTC-like layer  
 371 approaches the dimensionality of human VTC (TDANN mean = 13.2). However, the dimensionality of models trained  
 372 with  $SL_{Abs}$  decreases too quickly (mean = 6.5), and categorization-trained models remain higher than human VTC  
 373 at this level of  $\alpha$  (mean = 42.7).

374 We conclude that the close match between the TDANN and human VTC, on both topographic and non-topographic  
 375 benchmarks, may be due in part to an alignment of their intrinsic dimensionality. Similar results are observed  
 376 when summarizing the response eigenspectrum with power law fits, as in Stringer et al. [85], Kong et al. [82]  
 377 (Supplementary Figure S13c). Intriguingly, we find that the effective dimensionality of the TDANN roughly converges  
 378 to a common value of approximately 15 across model layers at  $\alpha = 0.25$  (Figure 6d), raising the possibility that a  
 379 similar dimension stabilization phenomenon occurs across brain areas in the ventral stream. These results provide  
 380 new evidence that the computational constraints generating cortical topography strongly influence *non-topographic*  
 381 *features*, making them more brain-like by virtue of decreasing the dimensionality of population responses.

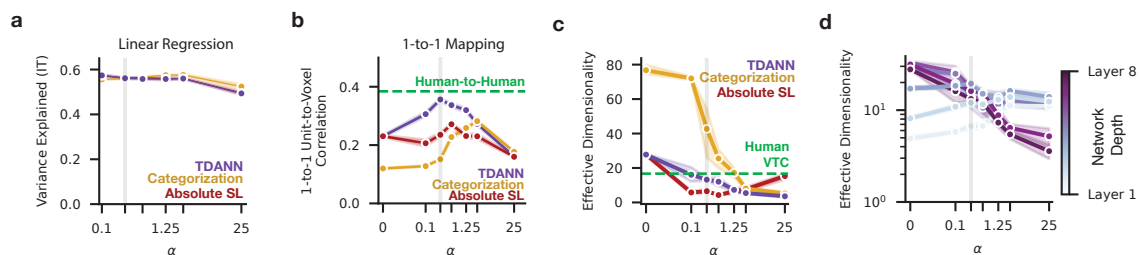


**Figure 6. Spatial constraints make learned representations more brain-like and reduce intrinsic dimensionality (a)** Variance explained under a linear regression mapping between model units and macaque IT neurons, as a function of the spatial loss weight  $\alpha$  and the training objective. **(b)** Mean correlation between model units and VTC voxels under a one-to-one mapping as a function of  $\alpha$ . Green: mean human-to-human correlation under the same one-to-one mapping. **(c)** Estimated effective dimensionality (cf. Elmoznino and Bonner [83], Del Giudice [84]) of the population response in the VTC-like layer of models trained at different levels of  $\alpha$  and with different objectives. Green: mean value in human VTC from the NSD dataset. **(d)** Effective dimensionality in the TDANN across all layers and levels of  $\alpha$ . In all panels, shaded vertical bar indicates value of  $\alpha$  demonstrated in prior analyses to best match topographic phenomena.

### 382 The TDANN minimizes inter-layer wiring length

383 Identifying the optimization paradigm that is most consistent with neural data provides insight into the constraints  
 384 underlying neural development, but prompts a deeper question: why would these constraints be favored by  
 385 evolutionary selection? A natural hypothesis is that cortical networks with strong functional organization also  
 386 minimize wiring length, and thus reduce brain size, weight, and power consumption [86, 18]. We test this hypothesis  
 387 by asking whether the optimization paradigm that generated a functional organization that best fit neural benchmarks  
 388 – intermediate spatial weight  $\alpha$ , self-supervised learning, and spatial costs that scale with cortical surface area –  
 389 also reduces between-layer wiring length. In feedforward networks that lack intra-layer connectivity, such as the  
 390 TDANN, any gains in wiring efficiency must be between layers. Accordingly, we measure inter-layer wiring length by  
 391 identifying populations of co-activated units in adjacent layers, then estimating the length of fibers needed to connect  
 392 those populations. We first present natural images to the network and record the locations of the most responsive  
 393 units in each layer, then simulate fiber bundles that originate in an earlier "source" layer and terminate in the following  
 394 "target" layer, adding inter-layer fibers until the total squared distance between each activated unit and its nearest  
 395 fiber is below a specified threshold (see Methods, Figure 7a). The total wiring length is taken as the sum of the  
 396 lengths of each fiber.

397 Presenting the TDANN with natural images leads to clustered responses in the VTC-like layer of all models trained  
 398 with  $\alpha > 0$ , with multiple clusters apparent at higher levels of  $\alpha$  (Supplementary Figure S14). Does the increase in  
 399 clustering within layers result in shorter wiring length between layers? We find that inter-layer wiring length is indeed  
 400 minimized at higher levels of  $\alpha$  (Figure 7b). However, we also find that object categorization performance decreases  
 401 as wiring efficiency improves (Figure 7c), indicating that models at low-to-intermediate levels of  $\alpha$  optimally balance  
 402 performance with inter-layer wiring efficiency. This coincidence of optimal  $\alpha$  values suggests that the functional  
 403 organization of the ventral visual stream balances inter-area wiring costs with performance. Critically, we find  
 404 that wiring is most efficient for the optimization objectives that yield the most brain-like functional organization:  
 405 wiring length is higher in both categorization-trained models and those trained with the Absolute SL (Figure 7d).

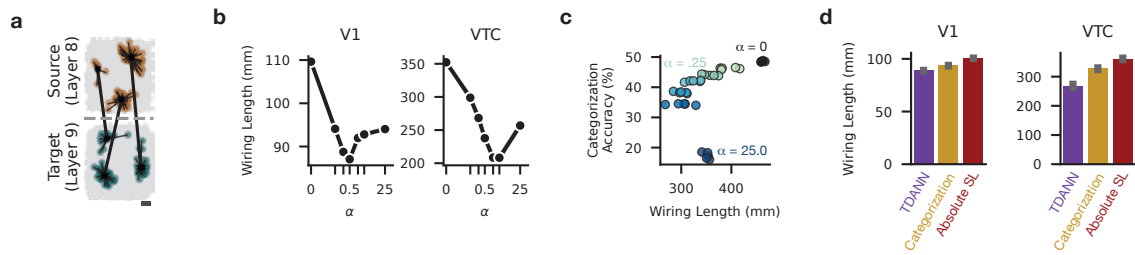


**Figure 7. Minimization of inter-layer (feedforward) wiring length in models with brain-like functional organization.** (a) Example wiring length computation between adjacent layers. Units in brown are the top 5% most active units in the Source layer for an arbitrarily-selected natural image, while units in green are the top 5% most active in the Target layer. Black dots show the origination and termination points of fibers that would be required to connect populations of active units across layers. (b) Wiring length between layers 4 and 5 ("V1"; left), and layer 8 and 9 ("VTC", right) as a function of  $\alpha$ . Shaded regions: 95% CI of measurements from different cortical neighborhoods, model seeds, and input images. (c) Accuracy on object categorization vs total wiring length, for models trained at different levels of  $\alpha$ . (d) Wiring length in both early and later model layers for models trained with different task and spatial objectives ( $\alpha = 0.25$  for all). Error bar: 95% CI over different image presentations and model seeds.

406 Thus, wiring length minimization provides a normative explanation for the superiority of self-supervised learning and  
 407 area-normalized spatial constraints.

#### 408 **Proof-of-principle: Using the TDANN as a digital twin for experimental design**

409 A quantitatively accurate and mechanistically grounded model of functional organization, such as the TDANN,  
 410 enables a spectrum of applied use cases that rely on estimating the effects of spatially-modulated neural  
 411 perturbations. Here we apply TDANN as a digital twin of visual cortex and demonstrate two novel applications:  
 412 1) performing an *in silico* microstimulation experiment, and 2) proof-of-principle for prototyping a simple cortical  
 413 prosthetic device.

414 **Simulated microstimulation reveals functional similarity of connected unit populations** Microstimulation experiments  
 415 in the macaque [87] found that stimulating neurons in a face patch selectively drives activity in other face patches,  
 416 and prior work with topographic models of macaque IT [78] found a similar result. We tested if the TDANN also  
 417 captures this connectivity by stimulating local populations of units in the penultimate model layer and recording  
 418 evoked responses in the following VTC-like layer. Mirroring results in macaque IT, we find that stimulating units  
 419 in a TDANN face patch drives localized activity in a face patch in the following layer (Figure 8a). We repeat the  
 420 stimulation for 99 other sites equally spaced on the simulated cortex, and find that the selectivity of a stimulated unit  
 421 in the source layer strongly predicts the selectivity of activated units in the target layer (Figure 8b), especially for  
 422 stimulation sites closer to the center of the simulated cortical tissue.

423 **Simulation of cortical prosthetic devices with TDANNs** A unique advantage of a unified topographic model such  
 424 as TDANN is that it can be used to prototype the effects of simultaneous stimulation of multiple cortical areas,  
 425 experiments which are challenging to perform *in vivo*. Based on recent advances in machine learning and  
 426 visual cortical prostheses [88, 89, 90], we introduce a framework using TDANNs to prototype multi-region cortical  
 427 stimulation devices. The framework has two components (Figure 8c, d): 1) a Stimulation Simulator that transforms  
 428 desired activity patterns on the cortical sheet into *device-achievable* patterns, and 2) a Percept Synthesizer that  
 429 estimates the percept evoked by stimulation with those patterns.

430 The Stimulation Simulator takes an input image, uses the TDANN to predict the precise pattern of responses in each  
 431 layer, and then constrains that pattern into one that is physically achievable by a specific hypothetical stimulation  
 432 device (Figure 8c). We model two kinds of physical constraints: spatial precision – the resolution at which the device  
 433 can create activity patterns, and regional access – the subset of cortical areas that are accessible to the device.  
 434 Spatial precision is modeled as a Gaussian blur of the desired activity pattern and regional access by restricting the  
 435 model layers that participate in the simulation.

436 To synthesize percepts from device achievable patterns, we use an approach inspired by Granley et al. [90] and  
 437 Shahbazi et al. [91] to synthesize the input image which generates the target activity pattern – i.e., a neural  
 438 metamer. Figure 8e illustrates predicted percepts for hypothetical cortical stimulation devices with variable precision  
 439 and access. Unsurprisingly, a device with infinitely high spatial stimulation precision yields sharp percepts even  
 440 when only early cortical areas are stimulated (Figure 8e, top left). However, the percepts quickly deteriorate as the  
 441 spatial precision of the device decreases (Figure 8e lower left). Notably, our simulation suggests that, at lower spatial

442 precision, the quality of percepts can be improved by adding stimulation of higher cortical areas (Figure 8e, middle  
443 rows).

444 While we have neglected many critical details here, including spatiotemporal processing, cortical magnification, and  
445 the need to validate percepts, we hope that this proof of principle motivates the use of TDANN to make testable  
446 predictions about the nature of percepts elicited by various cortical stimulation devices.

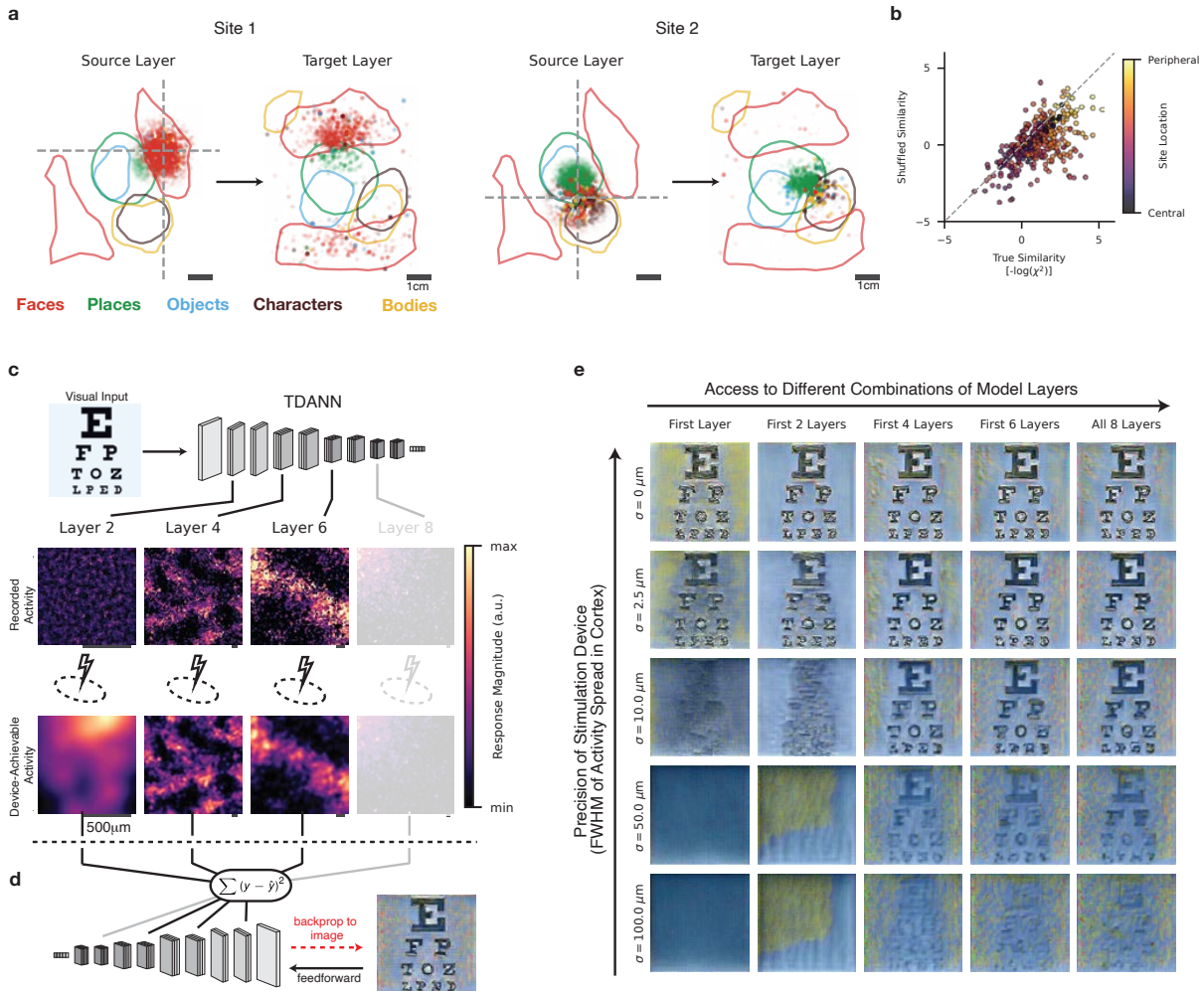


**Figure 8. Using TDANNs to simulate spatial stimulation devices.** (a) Stimulation of a local population of units in the second to last convolutional layer drives spatially-localized responses in the final convolutional layer. Responses are functionally aligned, such that stimulating face-selective units (Site 1) drives activity in face-selective units in the following layer. Right: Results for a second stimulation site, at the intersection of place-, body-, and character-selective patches. (b) Similarity in tuning of stimulated units in the source layer and responding units in the target layer for 100 evenly-spaced stimulation sites. Each dot compares tuning similarity for the true distribution of activated units (x-axis) and a randomly shuffled selection of units (y-axis). Dot color: distance of the stimulation site from the center of the cortical tissue. (c-d) Conceptual framework for applying the TDANN to the prototyping of visual cortical prostheses. (c) Stimulation Simulator: the TDANN is used to generate predicted activity patterns from a given visual input (top row). Patterns are then degraded according to the limitations on a hypothetical stimulation device: reduced spatial precision results in blurring of the target activity pattern (bottom row), and limits to regional access restrict the set of layers that participate. Here, Layer 8 is faded-out to show that this particular hypothetical device cannot reach that cortical area. (d) Given a device-achievable stimulation pattern produced by the Stimulation Simulator in (c), we synthesize the image that could evoke that pattern: the predicted percept. To build intuition for the fidelity of predicted percepts, we use an example input image of the the first four lines of a Snellen eye chart. (e) Predicted percepts for 25 theoretical cortical stimulation devices with different capabilities. Devices vary in the precision with which they are able to produce desired activity patterns (full-width at half-maximum (FWHM) of the spread of activity on cortex increases with rows) and the number of cortical areas that can be simultaneously simulated (columns).

## 447 Discussion

448 In this work, we leveraged the neural network modeling framework to seek the principles of functional organization  
449 in the primate ventral visual stream. We found that training a spatially-augmented deep neural network for a specific  
450 combination of objectives results in a model, the TDANN, that captures topographic properties throughout the ventral  
451 stream, from the pinwheels of V1 to the category-selective patches of higher-level visual cortex.

452 We identified two specific factors critical to the emergence of brain-like functional organization. First, we found  
453 that self-supervised learning of task-general representations yields better organization than the more common  
454 alternative of supervising on the singular task of visual object recognition. Recent work has suggested that functional  
455 specialization in the brain – e.g., one population of units responsible for discrimination of different faces and another  
456 for recognition of different objects – arises under joint training for two different supervised recognition tasks, one for  
457 faces and one for objects [92]. Our results demonstrate that functional specialization can emerge under a single  
458 unsupervised learning objective on a single training set, suggesting that general mechanisms can produce the  
459 kinds of functional specialization that is typically assumed to require multiple objectives or multiple distinct datasets.  
460 Second, we found that the spatial constraint in our model should compare response similarity and physical similarity  
461 according to a metric that scales with the size of each cortical area, rather than being fixed for all cortical areas.  
462 This finding suggests that the actual circuits responsible for shaping the structure of local response correlation in  
463 cortical neighborhoods should scale with the surface area of each cortical region. Our identification of these two  
464 critical factors demonstrates that a goal-driven modeling approach to understanding neural sensory systems can  
465 yield concrete and specific insights into their underlying principles.

466 Critically, the two factors that we found are essential for brain-like functional organization in the visual system are  
467 not specific to the visual modality, and might extend to predict the abundant, yet largely unexplained, functional  
468 organization in other sensory systems. For example, neurons in primary auditory cortex are arranged according  
469 to the frequency they respond most strongly to (tonotopy [2]), and in secondary auditory areas, neurons cluster  
470 according to their preference for speech and music [23, 93]. It is possible that the representations carried by these  
471 neurons are also learned by contrastive self-supervision, and that their topographic organization is explained by  
472 scalable spatial constraints of the forms described here. Likewise, the functional organization of somatosensory [4],  
473 entorhinal [6, 5] and parietal cortices [3] may be explained by the specific yet general principles for representation  
474 learning and spatial smoothness that we have identified. Under this hypothesis, it is only the structure of the input  
475 data (e.g., auditory experience, somatosensory input) that changes, but the cortical mechanisms for learning and  
476 organization remain universal across cortical systems. Future work can directly test that hypothesis by training  
477 TDANN variants to learn spatially-organized representations specific to each system.

478 The TDANN is the first model to predict functional organization in multiple cortical areas by learning features and  
479 topography, from scratch, in an end-to-end optimization framework trained directly on image inputs. As such, it  
480 represents an improvement over a number of related prior approaches. For example, hand-crafted self-organizing  
481 maps (SOMs) [94, 8, 10, 11, 9] have simplified the problem of topographic map formation by modeling a limited set  
482 of fixed feature dimensions (e.g., orientation preference and spatial frequency tuning), then modifying the tuning of  
483 model units along these dimensions such that nearby units develop similar selectivity. While such SOMs produce  
484 qualitatively smooth V1-like orientation maps, we find that they fail to quantitatively predict the topographic properties  
485 of V1 orientation maps (Figure 2). Recent attempts to abandon hand-crafted feature dimensions have trained  
486 SOMs to smoothly map the outputs of categorization-pretrained DCNNs [12, 13]. While these DNN-SOMs have  
487 the advantage of operating on images rather than predefined features, we find that they are quantitatively less  
488 accurate than the TDANN (Figure 3) at explaining the functional organization of VTC, and fail to reproduce the  
489 topography of V1 (Figure 2). Another recent approach, the ITN [20], appended topographic layers to a pretrained  
490 DCNN backbone and trained for supervised categorization under an additional wiring length minimization constraint.  
491 While the ITN reproduces many features of VTC topography, it does not predict the size, number, and geometry  
492 of category-selective patches as accurately as the TDANN, and cannot predict the functional organization of areas  
493 outside VTC. Prior work from our groups also followed the TDANN optimization framework, but used a supervised  
494 categorization task, a spatial constraint that did not scale with cortical area, and applied only to the VTC-like layer  
495 [78]. While this model was able to predict many properties of the functional organization of macaque IT, it is incapable of  
496 predicting the organization of other ventral stream regions. Our present results (Figure 5) demonstrate that different  
497 spatial and task objectives are required for a TDANN to accurately match the functional organization of multiple areas  
498 of the ventral visual stream.

499 That the TDANN is trained end-to-end provides two interesting opportunities for understanding the interaction  
500 between learned representations and functional organization during development. First, our preliminary analyses  
501 suggest that trajectories of TDANN functional architecture throughout training roughly match the faster development



502 of earlier vs higher cortical regions (Figure S17) and the emergence of V1-like topography from retinal wave-like  
503 stimuli (Figure S18). Rigorously testing those predictions would be most interesting when the TDANN is optimized  
504 using naturalistic movie streams that match the visual statistics and acuity limitations of human development [95, 96].  
505 Second, we found that the presence of the spatial constraint during training modulated the nature of learned  
506 representations, making them more brain-like and stabilizing their intrinsic dimensionality (Figure 6).

507 While the TDANN is the first unified model of ventral stream functional organization, it has a number of important  
508 limitations. Because the core DCNN architecture used in this work is strictly feedforward, there are no direct  
509 connections between different units in the same layer. Thus, we are only able to draw inferences about how the  
510 spatial constraint affects wiring length between layers. A more complex architecture could include both intra-layer  
511 recurrence and long-range feedback connections [97], although our results demonstrate that explicitly modeling  
512 these recurrent connections is not necessary to produce accurate topographic maps (see Figure 6 of Blauch et al.  
513 [20]), raising the possibility that minimization of the length of long-range fibers may be the key determinant of the  
514 functional organization of visual cortex.

515 We also note that our model, like all convolutional neural networks, uses the same filter weights across the entire  
516 visual field (termed "weight sharing"). This short-cut makes large-scale network training feasible; however, it is  
517 biologically implausible and potentially interferes with topographic map formation, since changing input weights to a  
518 unit in one part of the cortical sheet will also change the weights of many other distant units in a non-local fashion.  
519 Some topographic models avoid this issue by forgoing the use of convolutional layers altogether, but in doing so  
520 forfeit the ability to model retinotopically-organized cortical areas. In contrast, our approach is to pre-optimize unit  
521 positions (see Methods) in a way that allows the learning of locally-smooth topographic maps even with convolutional  
522 layers (see Methods). In the brain, a similar pre-optimization may be achieved by chemical gradients [98] and  
523 experience-independent refinement of neural circuits during embryonic development[99, 100, 101, 102].

524 Finally, an exciting application of the TDANN is the simulation of experiments with spatial manipulations and readouts  
525 (Figure 8). Virtually every experiment that uses topographic structure as a dependent variable, including controlled  
526 rearing and task learning paradigms, could first prototype experiments with TDANNs. In addition, experiments that  
527 involve inactivation or stimulation of local populations of neurons (e.g. Rajalingham and DiCarlo [103], Shahbazi  
528 et al. [91]) could use the TDANN to predict the downstream behavioral impact of those manipulations prior to  
529 collecting data. The tools to perform stimulation or inactivation of neural populations have become commonplace in  
530 systems neuroscience in the past decade, but their engagement with the strongest models of neuronal function –  
531 task-optimized neural networks – has been limited due to the lack of image-computable models that not only explain  
532 the responses of individual neurons [104, 105, 106, 25] but that are also mapped to cortical tissue. As a unified  
533 model of functional organization, the TDANN is well-suited to bridge this gap.

## 534 Methods

### 535 Code and data availability

536 Code for model training and analyses is available at <https://github.com/neuroailab/TDANN>.

### 537 Neural network architecture and training

538 **Model training.** We build off of the *torchvision* implementation of ResNet-18 [59] and train models with modifications  
539 to the VISSL framework [107]. All models were trained for 200 epochs of the ILSVRC-2012 (ImageNet Large-Scale  
540 Visual Recognition Challenge; Deng et al. [64]) training set. Unless otherwise indicated, models were each trained  
541 from five different random initial seeds. Network parameters were optimized with stochastic gradient descent with  
542 momentum ( $\gamma = 0.9$ ), a batch size of 512, and a learning rate initialized to 0.6 then decaying according to a  
543 cosine learning schedule [108]. Models were trained either for supervised 1000-way object categorization or on the  
544 self-supervised contrastive objective "SimCLR" [63]. Following training, categorization accuracy for self-supervised  
545 models was assessed by freezing the parameters of the model and training a linear readout from the outputs of the  
546 final layer. The linear readout is trained for 28 epochs with a batch size of 1,024 and a learning rate initialized to 0.04  
547 and decreasing by a factor of 10 every eight epochs.

548 **Initialization of model unit positions.** Prior to training, model units in each layer are assigned fixed positions in a  
549 two-dimensional cortical sheet that is specific to that layer. For efficiency, we do not embed the units of the very  
550 first convolutional layer. The size of the cortical sheet in each layer depends on a mapping between model layers  
551 and regions in the human ventral visual pathway, as well as a commitment to the extent of the visual field being  
552 modeled. For example, because we map model Layer 4 to human V1, the surface area of the cortical sheet in that  
553 layer is set to  $13\text{cm}^2$ : the mean value reported by Benson et al. [109] for the surface area of the section of human  
554 V1 that is sensitive to the central 7 degrees of visual angle. Another critical parameter in our framework is the size  
555 of a "cortical neighborhood": during training, computation of the spatial loss is restricted to units within the same  
556 cortical neighborhood. We set the neighborhood width to match measurements made of the spatial extent of lateral  
557 connections in different cortical areas of the macaque (from Yoshioka et al. [110]), then scale up to achieve estimates  
558 that might match the human ventral visual pathway. Table 1 details the sizes of simulated cortical sheets and cortical  
559 neighborhoods in all layers.

Layer	# Units	Size of Cortical sheet	Neighborhood Size	Region
Layer 2	200704	$5.7\text{mm}^2$	$47\mu\text{m}$	Retina
Layer 3	200704	$5.7\text{mm}^2$	$47\mu\text{m}$	Retina
Layer 4	100352	$13.5\text{cm}^2$	$1.6\text{mm}^*$	V1
Layer 5	100352	$13.5\text{cm}^2$	$1.6\text{mm}^*$	V1
Layer 6	50176	$12\text{cm}^2$	$4\text{mm}$	V2
Layer 7	50176	$5\text{cm}^2$	$2.5\text{mm}$	V4
Layer 8	25088	$49\text{cm}^2$	$31\text{mm}$	VTC
Layer 9	25088	$49\text{cm}^2$	$31\text{mm}$	VTC

**Table 1.** Parameters for layer positions. \*the value of 1.6mm used in the V1-like layer is known to be inaccurate, but matching the proper value yields too few units in each cortical neighborhood to compute pairwise distances. See Supplementary Figure S5 for a solution to this problem.

560 Positions are assigned in a two-stage process:

561 **Stage 1: Naive Retinotopic Initialization** Because each layer performs a convolution over the previous layer's  
562 outputs, responses are organized into spatial grids. We preserve this intrinsic organization by assigning each model  
563 unit to a region of the simulated cortical sheet that corresponds to its spatial receptive field.

564 **Stage 2: Pre-optimization of positions** Convolutional networks share filter weights between units at different  
565 locations; thus, local updates to a single unit entail updates to all units with the same filter weights. It is highly  
566 unlikely that an arbitrary configuration of unit positions will permit local smoothness under this global coordination  
567 constraint. Thus, we perform pre-optimization of unit positions to identify a set of unit positions for which learning  
568 smooth cortical maps is possible. Specifically, we spatially shuffle the units of a pre-trained DCNN on the cortical  
569 sheet such that nearby units have correlated responses to a set of sine grating images. The choice of sine gratings  
570 here is inspired by observations that edge-like propagating retinal waves drive experience-independent organization  
571 of the visual system in primates and other mammals [99, 100, 101, 102].

572 The spatial shuffling works as follows: 1) Select a cortical neighborhood at random. 2) Compute the pairwise  
573 response correlations of all units in the neighborhood. 3) Choose a random pair of units, and swap their locations  
574 in the cortical sheet. 4) If swapping positions decreases local correlations (measured as an increase in the Spatial  
575 Loss function described below), undo the swap. 5) Repeat steps 3-4 500 times. 6) Repeat steps 1-5 10,000 times.

576 **Loss functions.** We use two kinds of loss functions: spatial losses that encourage topographic structure, and task  
577 losses that encourage the learning of visual representations. We detail each in turn below:

578 **Spatial loss** The spatial loss (SL) function encourages nearby pairs of units to have response profiles that are  
579 more correlated with one another than those of distant units. Consider a neighborhood with  $N$  units. The vector of  
580 pairwise Pearson's response correlations,  $\vec{r}$ , has length  $M = \binom{N}{2}$ , the number of unique pairs. Let the corresponding  
581 vector of pairwise Euclidean cortical distances be denoted  $\vec{d}$ .

582 We define two SL variants:

$$SL_{\text{Abs}} = \frac{1}{M} \sum_{i=1}^M |r_i - D_i|, \quad (2)$$

$$SL_{\text{Rel}} = 1 - \text{Corr}(\vec{r}, \vec{D}), \quad (3)$$

583 where  $\text{Corr}$  is the Pearson's correlation function and  $\vec{D}$  is the inverse distance:

$$D_i = \frac{1}{d_i + 1} \quad (4)$$

584 **Task loss** The task loss is computed from the output of the final model layer. We use two task losses: the  
585 object categorization cross-entropy loss used in supervised object recognition (e.g. Krizhevsky et al. [111]) and  
586 the self-supervised SimCLR objective [63].

587 **Combination of losses during training** On each batch, model weights are updated to minimize a weighted sum of  
588 the task loss and the spatial loss contributed by each layer:

$$\text{TDANN Loss} = L_{\text{task}} + \sum_{k \in \text{layers}} \alpha_k SL_k \quad (5)$$

589 where  $\alpha$  is the weight of the spatial loss.

590 **Overview of Training** In summary, models are trained in 6 steps:

- 591 1. ResNet-18 is trained on the task loss only.
- 592 2. Positions in each layer are initialized to preserve coarse retinotopy (Stage 1).
- 593 3. Positions are further pre-optimized in an iterative process that preserves retinotopy while bringing together  
594 units with correlated responses to sine gratings images (Stage 2).
- 595 4. Positions are frozen and never again modified.
- 596 5. All network weights are randomly re-initialized.
- 597 6. The network is trained to minimize a weighted combination of the spatial and task loss components.

598 **Benchmarks comparing macaque V1 to model V1-like layers**

599 **Stimuli and Tuning Curves.**

600 **Sine Grating Images** Tuning to low-level image properties such as orientation, spatial frequency, and chromaticity  
601 was assessed by constructing  $224 \times 224$  pixel sine grating images that span 8 orientations evenly spaced between  
602 0 and 180 degrees, 8 spatial frequencies between 0.5 and 12 cycles per degree, 5 spatial phases, and two  
603 chromaticities: black/white gratings and red/cyan gratings.

604 **Tuning Curves** We evaluated tuning for orientations and spatial frequencies by constructing tuning curves for each  
605 unit. Color-responsiveness is assessed by comparing the mean response to all black and white gratings to the mean  
606 response to all red/cyan gratings. The distribution of model unit activations for a given layer was rescaled to match  
607 the minimum and maximum firing rates reported in [34]. We quantify the orientation tuning strength of model units  
608 using circular variance (CV), where values closer to 0 correspond to sharper tuning. As in Ringach et al. [34], CV is  
609 defined as:

$$CV = 1 - \left| \frac{\sum_k r_k e^{i2\theta_k}}{\sum_k r_k} \right| \quad (6)$$

610 Where  $\theta_k$  is the  $k$ th orientation, in radians, and  $r_k$  is the scaled response to that orientation. Orientation tuning  
611 curves are additionally fit with a von Mises function whose peak is taken as the preferred orientation.

## 612 **Models.**

613 **Hand-Crafted Self-Organizing Map** Our hand-crafted self-organizing map (SOM) implementation uses the *MiniSom*  
614 library [112], with parameters adapted from Swindale and Bauer [11]. We instantiate the SOM as a 128 x 128 grid  
615 of model units.

616 10,000 training samples were randomly constructed by selecting a random (x, y) location, orientation ( $[0, \pi]$ ), spatial  
617 frequency ( $[0, 1]$ ), and chromaticity (black/white, colorful).

618 As in Swindale and Bauer [11], SOM weights were initialized retinotopically with randomly-selected initial preferred  
619 orientations.

620 The SOM is trained by presenting training examples for a total of 700,000 updates. After each example, the "winning"  
621 unit (i.e. the one with the highest response) is updated with a learning rate of  $\epsilon = 0.02$  to be more strongly aligned  
622 with the input stimulus, and its neighbors are updated in proportion to their proximity to the winner, as determined by  
623 a Gaussian neighborhood function parameterized by  $\sigma = 2.5$ .

624 Following training, each sine grating in the set of probe stimuli is presented to the SOM by projecting it into the  
625 six-dimensional space of SOM unit tuning and computing the response of each SOM unit to the stimulus. Once  
626 responses to each stimulus are obtained, tuning curves are constructed as usual.

627 **DNN-SOM** The DNN-SOM is identical to the hand-crafted SOM, except that 1) the inputs are derived from the  
628 outputs of the first layer of an AlexNet model pretrained for ImageNet object categorization and 2) the learning rate is  
629 increased, which we found helps convergence. Following the approach of Zhang et al. [12], we take the responses of  
630 the first AlexNet layer to all 50,000 natural images in the ImageNet dataset, reduce their dimensionality with principal  
631 components analysis, and train the SOM on those examples.

632 **Response Benchmarks.** Model responses are compared to macaque V1 by considering preferred orientations and  
633 orientation tuning strength. Orientation tuning strength is computed as circular variance (CV) and compared  
634 between the population of model units and the empirical distribution provided by Ringach et al. [34] with the  
635 Kolmogorov-Smirnov distance. To filter out noisy units, we compute CV for model units with a mean response  
636 magnitude of at least 1.0. The distribution of preferred orientations is also compared to empirical data collected by  
637 De Valois et al. [35] by counting the number of units preferring each of four orientations: 0, 45, 90, and 135 degrees.  
638 In Figure S3b we compute a "Cardinality Index": the fraction of preferred orientations that include, 0, 90, and 180  
639 degrees.

640 **Topographic Benchmarks.** Orientation preference maps (OPMs) are compared to empirical measurements in two  
641 ways: counting pinwheels and quantifying map smoothness.

642 **Pinwheel Detection** We interpolate the OPM onto a two-dimensional grid by computing the circular mean of the  
643 preferred orientation of units near a given location. If the population of model units near a grid location has  
644 high heterogeneity in preferred orientation, we disqualify that pixel for having an unreliable estimate of preferred  
645 orientation. Each grid location is assigned a "winding number" [17], computed by considering the preferred  
646 orientations of the eight pixels directly bordering the pixel under consideration. Moving clockwise around the  
647 bordering eight pixels, the change in preferred orientation from pixel to pixel is summed. A high winding number  
648 indicates a clockwise pinwheel, and a low winding number indicates a counterclockwise pinwheel, where the  
649 thresholds for "high" and "low" are selected to be consistent with manual annotation of clear pinwheels.

650 **Pairwise Tuning Difference** We compute the smoothness of orientation preference maps by constructing a curve  
651 relating pairwise difference in preferred orientation to pairwise cortical distance. First, we restrict the population of  
652 model units to those with the highest 25% peak-to-peak tuning curve magnitudes. This filtering step removes units  
653 with weak responses or responses that would be indistinguishable from a "cocktail blank" background activity level,  
654 and we consider it equivalent to neuron selection in electrophysiological and optical imaging studies [34, 43]. As in  
655 similar approaches to quantifying OPM structure (e.g. Chang et al. [68]), pairs of units are binned according to their  
656 distance, and the average absolute difference in preferred orientation is plotted for each distance bin. Because there  
657 can be hundreds of thousands of units in a given layer, we restrict this analysis to randomly-selected neighborhoods  
658 of a fixed width, then sample many neighborhoods from each map. Finally, we divide the pairwise distance by the  
659 chance value obtained by random resampling of unit pairs, such that a values  $< 1$  indicate more similar tuning than  
660 would be expected by chance.

661 The OPM curves are compared to reconstructed macaque V1 data from Nauhaus et al. [43].

662 We adopt an identical approach for the construction of a neural spatial frequency preference map, where data are  
663 also provided for the same imaging window in Nauhaus et al. [43]. A similar strategy was used to recover data on  
664 cytochrome oxidase (CO) uptake from Livingstone and Hubel [38].

665 **Smoothness** We define a smoothness score for a given map by comparing the tuning similarity for the nearest  
666 model unit pairs to the tuning similarity of the least similar pairs. Concretely, given a vector  $x$  of pairwise tuning  
667 similarity values, sorted in order of increasing cortical distance:

$$S(x) = \frac{\max(x) - x_0}{x_0} \quad (7)$$

## 668 **Benchmarks comparing human VTC to model VTC-like layers**

669 **Stimuli.** We evaluate the selectivity of neurons and model units to visual object categories using the "fLoc" functional  
670 localizer stimulus set [76]. fLoc contains five categories, each with two subcategories consisting of 144 images  
671 each. The categories are faces (adult and child faces), bodies (headless bodies and limbs), written characters  
672 (pseudowords and numbers), places (houses and corridors), and objects (string instruments and cars). Selectivity  
673 was assessed by computing the  $t$ -statistic over the set of functional localizer stimuli and defining a threshold above  
674 which units were considered selective.

$$t = \frac{\mu_{\text{on}} - \mu_{\text{off}}}{\sqrt{\frac{\sigma_{\text{on}}^2}{N_{\text{on}}} + \frac{\sigma_{\text{off}}^2}{N_{\text{off}}}}}, \quad (8)$$

675 where  $\mu_{\text{on}}$  and  $\mu_{\text{off}}$  are the mean responses to the "on" categories (e.g., adult and child faces) and "off" categories  
676 (e.g., all non-face categories), respectively,  $\sigma^2$  are the associated variances of responses to exemplars from those  
677 categories, and  $N$  is the number of exemplars being averaged over.

678 **Human Data.** We compare models to human data from the Natural Scenes Dataset (NSD) [75], a high-resolution  
679 fMRI dataset of responses to 10,000 natural images in each of eight individuals (see Allen et al. for details). Models  
680 are compared to two aspects of this dataset: single-trial responses to the main set of natural images per participant  
681 (see "One-to-one mapping") and selectivity in response to the "fLoc" stimuli. Single-trial responses were  $z$ -scored  
682 across images for each voxel and session and then averaged across three trial repeats. Selectivity was computed  
683 on the "fLoc" experiment as described in the previous section, generating  $t$ -maps for each of the five categories for  
684 each individual subject.

685 The VTC region of interest (ROI) was drawn based on anatomical landmarks to follow the convention in the literature  
686 [113] and is provided in the NSD data release as the "Ventral" ROI in the "streams" parcellation.

## 687 **Models.**

688 **Interactive Topographic Network (ITN)** We reconstruct maps from a variant of the ITN in Blauch et al. [20] that was  
689 trained and evaluated on the same images as the remaining models.

690 **DNN-SOM** Two related approaches for building SOM models of higher visual cortex have recently been published  
691 [12, 13]. Because neither paper evaluates the resulting topographic maps with the fLoc stimuli, we reimplement  
692 the approach of Zhang et al. [12] as follows. We extract the responses of each unit in the final layer of a pretrained  
693 AlexNet to all 50,000 images in the ImageNet validation set. The responses are then reduced to the first four principal  
694 components. The SOM is initialized as a 200 x 200 grid of model units with a Gaussian neighborhood function set  
695 to  $\sigma = 6.2$ . The learning rate is set to 1.0 and the SOM is trained for 200,000 total iterations. The fLoc images are

696 presented to the pretrained AlexNet model and projected into the space spanned by the four principal components  
 697 computed previously. The response of each model unit to each fLoc image is computed by taking the dot product of  
 698 the unit weight matrix with the projected fLoc images. The SOM is then treated identically to the VTC-like layer of  
 699 TDANN.

#### 700 **Response Benchmarks.**

701 **Representational similarity analysis** We compare functional properties of human VTC and models with  
 702 representational similarity analysis (RSA) [72]. For any given model or human hemisphere, we compute a  
 703 representational similarity matrix (RSM) as the pairwise Pearson's correlation between patterns of selectivity for  
 704 each of the five fLoc categories. The diagonal of the RSM is trivially 1.0 and is ignored in further analysis. The  
 705 similarity of two RSMs is computed as Kendall's  $\tau$ .

#### 706 **Topographic Benchmarks.**

707 **Pairwise Tuning Difference** We measure pairwise difference in VTC-like layer unit tuning as a function of cortical  
 708 distance. We draw 25 random samples of 500 units each. Each sample is filtered to include only units with a mean  
 709 response of at least 0.5 a.u.. For each fLoc category, the absolute pairwise difference in selectivity is computed  
 710 for pairs of units separated by different cortical distances. Curves are normalized by the chance value obtained by  
 711 randomly shuffling unit positions. Smoothness of maps is computed from these curves, same as in our analysis of V1.  
 712 To compare a model to a human hemisphere, we compute the mean category-by-category difference in smoothness,  
 713 e.g. comparing model face map smoothness to human face map smoothness, model body map smoothness to  
 714 human body map smoothness, etc. Permutation tests randomly assigning category-by-category smoothness profiles  
 715 to either "model" or "human" were used to assess the statistical significance of the mean difference in smoothness.

716 **Patch Count and Size** Patches are automatically detected in maps of category selectivity by identifying contiguous  
 717 regions of highly-selective units (or voxels, for human VTC). Patch identification has a small number of parameters  
 718 that can be adjusted for maps of different sizes and with different dynamic ranges of selectivity values. The first step  
 719 in identifying patches is to smooth and interpolate discrete selectivity maps. The selectivity map is then thresholded,  
 720 and contiguous islands surviving the threshold are retained as candidate patches. Each candidate patch is further  
 721 filtered for reasonable size: patches must be at least  $100mm^2$  and no larger than  $45cm^2$ . Finally, the 2D geometry  
 722 of the patch is constructed by fitting the concave hull of the points within the patch.

723 The following table identifies the relevant parameters for patch identification in human VTC and for each candidate  
 model class.

Model	Selectivity Threshold	Smoothing $\sigma$	Minimum Size square mm	Maximum Size square mm
Human VTC	4	None	100	None
TDANN	2	2.4	100	4500
ITN	8	0.7	100	4500
DNN-SOM	10	2.4	100	4500

724 **Table 2.** Patch detection parameters for human VTC and each model.

725 **Selectivity Overlap** We determine if units (or voxels, for human VTC) that are selective for a pair of categories  
 726 overlap with one another as follows. First, we bin the cortical sheet into discrete square neighborhoods of width  
 727 10mm. In each neighborhood, the fraction of units selective for Category X and Category Y are recorded. We  
 728 consider two populations as overlapping if there is a strong correlation between the proportions recorded across  
 729 neighborhoods, i.e., if the frequency of Category 1 selectivity is predictive of Category Y selectivity and vice-a-versa.  
 730 The X-Y Overlap score is computed as

$$\text{Overlap} = \frac{1 - \text{RankCorr}(X, Y)}{2}, \quad (9)$$

731 where RankCorr is the Spearman's rank correlation coefficient and  $\vec{X}$  is the proportion of units selective for Category  
 732 X in each cortical neighborhood. The category selectivity threshold was set at  $t > 4$ .

733 **Linear regression.** Neural predictivity is computed against a given dataset as the mean variance explained across  
734 neurons and splits of the data. In practice we follow the parameters and design decisions made by the BrainScore  
735 team [30]; they are repeated here for completeness. We use partial least squares (PLS) regression to predict the  
736 activity of a given neuron as a linear weighted sum of model units in a given layer. Model activations are preprocessed  
737 by first projecting unit responses to ImageNet images onto the first 1000 principal components, i.e. each component  
738 is a linear mixture of model units. This projection is used when fitting on the stimuli that were shown to the animal.  
739 When fitting IT, we use data from Majaj, Hong, et al., 2015 [32], which consists of multi-electrode array data in  
740 responses to quasi-naturalistic scenes with a variety of objects on a variety of backgrounds. Variance explained is  
741 corrected by dividing raw predictivity by the internal noise ceiling, a measure of the consistency of each recorded  
742 neuron.

### 743 **One-to-one mapping of visual cortical responses**

744 A direct, one-to-one mapping between units and voxels is computed by assigning each unit in a layer of the network  
745 to a single voxel based on responses to a given dataset. In practice, we correlate individual model unit activations to  
746 the natural images from the Natural Scenes Dataset [75] with responses to these same images on the single voxel  
747 level for a given subject. Unit-to-voxel assignments are determined using a polynomial-time optimal assignment  
748 algorithm [114] which maximizes the overall average correlation between unit and voxel pairs, on a given training  
749 set. The 515 shared images that all eight subjects viewed three times were held out as a test set and all reported  
750 one-to-one correlations are calculated on this test set, using the unit-to-voxel assignments determined from training.  
751 Each unit-to-voxel correlation is normalized by the individual voxel noise ceiling of that assigned voxel (see Allen et al.  
752 for information on the calculation of the intra-individual voxel noise ceilings in NSD). One-to-one correlations were  
753 calculated on an individual subject basis for each of the self-supervised and supervised models trained at each level  
754 of the spatial weight  $\alpha$ . The inter-individual, or subject-to-subject, noise ceiling, was calculated in the same manner,  
755 this time assigning voxels from one subject to voxels from another subject based on how correlated responses to  
756 the shared 515 images were for each potential voxel pair. For the subject-to-subject assignment, we used an 80/20  
757 train/test split and averaged results for each subject combination across 5 splits. A similar analysis will appear in a  
758 forthcoming publication by Finzi et al.

### 759 **Wiring Length**

760 We measure the functional wiring length between two adjacent layers, the "source" layer and the "target" layer by  
761 first identifying the units with the highest responses in each layer, then computing the length of inter-layer fibers that  
762 would be required to connect them. First, for a given natural image input, we identify the top  $p\%$  most responsive  
763 units in each of two adjacent layers. We set  $p$  to 5% in the V1-like layers and 1% in the VTC-like layers. We note  
764 that for computational tractability, we restrict our analysis to small neighborhoods in the V1-like layers and average  
765 results across many random neighborhood selections.

766 Next, inter-layer fibers are added one by one, until all activated units in the earlier "source" layer are sufficiently  
767 close to the location at which a fiber originates. In practice, we find the optimal fiber origination sites using the  
768  $k$ -means clustering algorithm, and continue adding fibers until the total "inertia" of the  $k$ -means clustering falls below  
769 a specified threshold,  $k_{\text{thresh}}$ . Inertia is computed as the sum of the squared distances between each activated unit  
770 and its nearest fiber, and  $k_{\text{thresh}}$  is set such that the mean distance from each unit to its nearest fiber is not greater  
771 than  $d_{\text{thresh}}$ .  $d_{\text{thresh}}$  is set to 10.0mm in the VTC-like layer pairs, and is reduced to 0.9mm in the V1-like layer pairs  
772 to reflect the smaller cortical neighborhood. Having established the number of inter-layer fibers required and their  
773 origination sites in the "source" layer, we identify optimal termination sites for those fibers in the "target" layer as  
774 follows. The set of target layer termination sites is identified as the centroids from  $k$ -means clustering, with  $k$  set to  
775 the number of fibers. Finally, fibers are assigned between origination sites and termination sites with the linear sum  
776 assignment algorithm, and the total wiring length is computed as the sum of the lengths of each individual inter-layer  
777 fiber.

778 A critical decision when measuring wiring length in this way is how to situate units from two layers in a common  
779 physical space. By design, each TDANN layer occupies a unique two-dimensional sheet, leaving the spatial  
780 relationships between units in different cortical sheets undefined. Here, we assume that the "source" cortical sheet  
781 and "target" cortical sheet lie in the same 2D plane, joined at one edge. Concretely, we can position the "target"  
782 sheet to the left, right, above, or below the "source" layer. Without reason to choose one of these strategies, we  
783 compute the optimal wiring length for each of the four options and report the average across all shift directions.

## 784 Dimensionality

785 In our analyses of dimensionality, we consider the responses of the full population of model units in each layer  
786 to a set of 10,112 natural images from the NSD [75]. Following [83], we perform spatial max-pooling on the  
787 convolutional feature maps, then compute the eigenspectrum of these responses. We summarize the dimensionality  
788 of the responses by their effective dimensionality (ED; Del Giudice [84]):

$$ED = \frac{\left(\sum_{i=1}^N \lambda_i\right)^2}{\sum_{i=1}^N \lambda_i^2}, \quad (10)$$

789 where  $\lambda_i$  is the  $i$ th eigenvalue, and  $N$  is the number of eigenvectors.

## 790 Microstimulation of model units on the simulated cortical sheet

791 We simulate the microstimulation of local populations of model units to 1) gain insight into the functional properties of  
792 local populations, and 2) measure effective connectivity between groups of units in adjacent layers. In all analyses,  
793 stimulation is performed by fixing the activity of units to values determined by a 2D Gaussian function. Units near  
794 the center of the Gaussian have their activity set to the maximal value, and activity falls off with distance from the  
795 center. We consider the top 5% of units, ranked by activity level, as being responsive in either the "Source" layer,  
796 where activity is set according to the 2D Gaussian, or in the following "Target" layer, where unit activity is determined  
797 by the network architecture and learned weights.

798 **Functional Alignment** In VTC-like layers, we measure functional alignment between layers by comparing the  
799 category selectivity of activated units in the Source layer (Layer 8) with the selectivity of responsive units in the  
800 Target layer (Layer 9). For each stimulation site, we compute the mean selectivity ( $t$ -statistic) of the top 5% most  
801 activated units for each of the following categories: faces, bodies, characters, cars, and places. This five-element  
802 "selectivity profile" can then be compared to the profile of the top 5% most strongly responding units in the Target  
803 layer by computing  $\chi^2$  distance between selectivity profiles. Similarity is then taken as the negative log distance and  
804 compared to a shuffle-control in which a random subset of units is compared instead of the top 5% most active units.

## 805 Simulation of a Visual Cortical Prosthesis

806 In Figure 8, we demonstrate a proof of concept for using topographic DCNNs to prototype visual cortical prosthetic  
807 devices. This proof of concept consists of two distinct stages: 1) generating device-achievable stimulation patterns  
808 with a Stimulation Simulator, and 2) generating the estimated percept (Percept Synthesizer) that would result  
809 by stimulating cortical areas with those patterns. To generate stimulation patterns, we feed a target image into  
810 TDANN and record the precise activation magnitude of each model unit in each layer. If an infinitely high-precision  
811 stimulation device with absolute coverage of the cortical sheet in all cortical areas were available, we would stimulate  
812 cortex with this set of precise activation patterns. However, real stimulation devices are limited in many ways,  
813 including limits to their spatial precision and the set of cortical areas they can access. Thus, we use TDANN  
814 to produce *device-achievable* stimulation patterns, i.e., those that are consistent with the limitations of cortical  
815 stimulation devices. Here we take a simple approach by considering degradation of high-precision patterns into  
816 device-achievable patterns by Gaussian blurring. In each layer, we first interpolate the precise activity patterns onto  
817 a high-resolution grid ( $2500 \times 2500$  px), then blur the resulting pattern with a 2D Gaussian kernel whose  $\sigma$  parameter  
818 is set according to the desired blur level. Because different layers have different cortical sheet sizes (e.g. 70mm  
819 on an edge in the VTC-like layer and 37mm on an edge in the V1-like layer), the width of the Gaussian in *pixels* is  
820 variable, even though the width of the Gaussian in *mm* is constant. Finally, we perform a nearest-neighbor lookup  
821 such that each model unit adopts the activity level of the pixel closest to its location. This set of activity patterns is the  
822 final "device-achievable" pattern. The Stimulation Simulator also allows any specific subset of layers to be included;  
823 e.g. the first two layers only, or all eight layers. We consider this restriction comparable to the limited access a neural  
824 stimulation device might be restricted to.

825 Given a set of device-achievable activity patterns, we seek to determine the estimated percept that would be evoked  
826 if that pattern were written into cortex, i.e., the visual input that is most consistent with those patterns. To this end, we  
827 follow the example of Granley et al. [90] and use gradient-ascent image optimization methods to synthesize an image  
828 such that the activity pattern produced by presenting that image is as close as possible to the device-achievable  
829 target pattern. We use the *lucent* Python package to iteratively optimize an image to minimize the total mean squared  
830 error, summed across layers, between the target activity patterns and the current evoked patterns at that iteration.  
831 We optimize the image for 3000 steps at a learning rate of 0.05; further optimization has little effect on reducing the  
832 mean squared error. The optimized result is the predicted percept for a given input image and theoretical cortical  
833 stimulation device.



## <sup>834</sup> **Author Contributions**

<sup>835</sup> E.M. and D.F. performed analyses. E.M., K.G.-S., and D.L.K.Y. wrote the paper. H.L., J.J.D., and D.L.K.Y. originally  
<sup>836</sup> conceived the approach.

## 837 **Acknowledgements**

838 This work was supported by a National Science Foundation Graduate Research Fellowship awarded to E.M., a  
839 National Institutes of Health grant (RO1 EY 022318) awarded to K.G.-S., a Simons Foundation grant (543061)  
840 awarded to D.L.K.Y., a National Science Foundation CAREER grant (1844724) awarded to D.L.K.Y., and an Office  
841 of Naval Research grant (S5122) awarded to D.L.K.Y. We also thank the NVIDIA corporation and the Google TPU  
842 Research Cloud group for hardware grants. We are grateful to Ben Sorscher for helpful discussions.

## 843 References

- 844 1. D H Hubel and T N Wiesel. Receptive fields, binocular interaction and functional architecture in the cat's visual  
845 cortex. *J. Physiol.*, 160:106–154, January 1962.
- 846 2. Colin Humphries, Einat Liebenthal, and Jeffrey R Binder. Tonotopic organization of human auditory cortex.  
847 *Neuroimage*, 50(3):1202–1211, April 2010.
- 848 3. B M Harvey, B P Klein, N Petridou, and S O Dumoulin. Topographic representation of numerosity in the human  
849 parietal cortex. *Science*, 341(6150):1123–1126, September 2013.
- 850 4. Y C Wong, H C Kwan, W A MacKay, and J T Murphy. Spatial organization of precentral cortex in awake  
851 primates. I. Somatosensory inputs. *J. Neurophysiol.*, 41(5):1107–1119, September 1978.
- 852 5. Horst A Obenhaus, Weijian Zong, R Irene Jacobsen, Tobias Rose, Flavio Donato, Liangyi Chen, Heping  
853 Cheng, Tobias Bonhoeffer, May-Britt Moser, and Edvard I Moser. Functional network topography of the medial  
854 entorhinal cortex. *Proc. Natl. Acad. Sci. U. S. A.*, 119(7), February 2022.
- 855 6. Yi Gu, Sam Lewallen, Amina A Kinkhabwala, Cristina Domnisoru, Kijung Yoon, Jeffrey L Gauthier, Ila R Fiete,  
856 and David W Tank. A Map-like Micro-Organization of Grid Cells in the Medial Entorhinal Cortex. *Cell*, 175(3):  
857 736–750.e30, October 2018.
- 858 7. Harry G Barrow, Alistair J Bray, and Julian M L Budd. A Self-Organizing Model of “Color Blob” Formation.  
859 *Neural Comput.*, 8(7):1427–1448, October 1996.
- 860 8. Teuvo Kohonen. Self-organized formation of topologically correct feature maps. *Biol. Cybern.*, 43(1):59–69,  
861 1982.
- 862 9. K Obermayer, H Ritter, and K Schulten. A principle for the formation of the spatial structure of cortical feature  
863 maps. *Proc. Natl. Acad. Sci. U. S. A.*, 87(21):8345–8349, November 1990.
- 864 10. Richard Durbin and Graeme Mitchison. A dimensionality reduction framework for understanding cortical maps.  
865 *Letters to nature*, 343:644–647, 1990.
- 866 11. N V Swindale and H Bauer. Application of Kohonen’s self-organizing feature map algorithm to cortical maps  
867 of orientation and direction preference. *Proceedings of the Royal Society of London B: Biological Sciences*,  
868 265(1398):827–838, May 1998.
- 869 12. Yiyuan Zhang, Ke Zhou, Pinglei Bao, and Jia Liu. Principles governing the topological organization of object  
870 selectivities in ventral temporal cortex. September 2021.
- 871 13. Fenil R Doshi and Talia Konkle. Visual object topographic motifs emerge from self-organization of a unified  
872 representational space. September 2022.
- 873 14. R Linsker. From basic network principles to neural architecture: emergence of orientation columns. *Proc. Natl.*  
874 *Acad. Sci. U. S. A.*, 83(22):8779–8783, November 1986.
- 875 15. K D Miller, J B Keller, and M P Stryker. Ocular dominance column development: analysis and simulation.  
876 *Science*, 245(4918):605–615, August 1989.
- 877 16. K D Miller. A model for the development of simple cell receptive fields and the ordered arrangement of  
878 orientation columns through activity-dependent competition between ON- and OFF-center inputs. *J. Neurosci.*,  
879 14(1):409–441, January 1994.
- 880 17. Miguel A Carreira-Perpiñán, Richard J Lister, and Geoffrey J Goodhill. A computational model for the  
881 development of multiple maps in primary visual cortex. *Cereb. Cortex*, 15(8):1222–1233, August 2005.
- 882 18. R A Jacobs and M I Jordan. Computational Consequences of a Bias toward Short Connections. *J. Cogn.*  
883 *Neurosci.*, 4(4):323–336, 1992.
- 884 19. A A Koulakov and D B Chklovskii. Orientation preference patterns in mammalian visual cortex: a wire length  
885 minimization approach. *Neuron*, 29(2):519–527, February 2001.
- 886 20. Nicholas M Blauch, Marlene Behrmann, and David C Plaut. A connectivity-constrained computational account  
887 of topographic organization in primate high-level visual cortex. *Proc. Natl. Acad. Sci. U. S. A.*, 119(3), January  
888 2022.

- 889 21. A Hyvärinen, P O Hoyer, and M Inki. Topographic independent component analysis. *Neural Comput.*, 13(7):  
890 1527–1558, July 2001.
- 891 22. T Anderson Keller, Qinghe Gao, and Max Welling. Modeling Category-Selective Cortical Regions with  
892 Topographic Variational Autoencoders. October 2021.
- 893 23. Alexander J E Kell, Daniel L K Yamins, Erica N Shook, Sam V Norman-Haignere, and Josh H McDermott. A  
894 Task-Optimized Neural Network Replicates Human Auditory Behavior, Predicts Brain Responses, and Reveals  
895 a Cortical Processing Hierarchy. *Neuron*, 98(3):630–644.e16, May 2018.
- 896 24. Daniel L Yamins, Ha Hong, Charles Cadieu, and James J DiCarlo. Hierarchical modular optimization of  
897 convolutional networks achieves representations similar to macaque IT and human ventral stream. *Adv. Neural  
898 Inf. Process. Syst.*, 26, 2013.
- 899 25. Daniel L K Yamins, Ha Hong, Charles F Cadieu, Ethan A Solomon, Darren Seibert, and James J DiCarlo.  
900 Performance-optimized hierarchical models predict neural responses in higher visual cortex. *Proc. Natl. Acad.  
901 Sci. U. S. A.*, 111(23):8619–8624, 2014.
- 902 26. Seyed-Mahdi Khaligh-Razavi and Nikolaus Kriegeskorte. Deep supervised, but not unsupervised, models may  
903 explain IT cortical representation. *PLoS Comput. Biol.*, 10(11):e1003915, November 2014.
- 904 27. Umut Güçlü and Marcel A J van Gerven. Deep Neural Networks Reveal a Gradient in the Complexity of Neural  
905 Representations across the Ventral Stream. *J. Neurosci.*, 35(27):10005–10014, July 2015.
- 906 28. Santiago A Cadena, George H Denfield, Edgar Y Walker, Leon A Gatys, Andreas S Tolia, Matthias Bethge,  
907 and Alexander S Ecker. Deep convolutional models improve predictions of macaque V1 responses to natural  
908 images. *PLoS Comput. Biol.*, 15(4):e1006897, April 2019.
- 909 29. Jonas Kubilius, Martin Schrimpf, Kohitij Kar, Rishi Rajalingham, Ha Hong, Najib Majaj, Elias Issa, Pouya  
910 Bashivan, Jonathan Prescott-Roy, Kailyn Schmidt, Aran Nayebi, Daniel Bear, Daniel L Yamins, and James J  
911 DiCarlo. Brain-Like Object Recognition with High-Performing Shallow Recurrent ANNs. In H Wallach,  
912 H Larochelle, A Beygelzimer, F Alche-Buc, E Fox, and R Garnett, editors, *Advances in Neural Information  
913 Processing Systems 32*, pages 12805–12816. Curran Associates, Inc., 2019.
- 914 30. Martin Schrimpf, Jonas Kubilius, Michael J Lee, N Apurva Ratan Murty, Robert Ajemian, and James J DiCarlo.  
915 Integrative Benchmarking to Advance Neurally Mechanistic Models of Human Intelligence. *Neuron*, September  
916 2020.
- 917 31. Martin Schrimpf, Idan Asher Blank, Greta Tuckute, Carina Kauf, Eghbal A Hosseini, Nancy Kanwisher,  
918 Joshua B Tenenbaum, and Evelina Fedorenko. The neural architecture of language: Integrative modeling  
919 converges on predictive processing. *Proc. Natl. Acad. Sci. U. S. A.*, 118(45), November 2021.
- 920 32. N J Majaj, H Hong, E A Solomon, and J J DiCarlo. Simple Learned Weighted Sums of Inferior Temporal  
921 Neuronal Firing Rates Accurately Predict Human Core Object Recognition Performance. *Journal of  
922 Neuroscience*, 35(39):13402–13418, 2015.
- 923 33. Beth L Chen, David H Hall, and Dmitri B Chklovskii. Wiring optimization can relate neuronal structure and  
924 function. *Proc. Natl. Acad. Sci. U. S. A.*, 103(12):4723–4728, March 2006.
- 925 34. Dario L Ringach, Robert M Shapley, and Michael J Hawken. Orientation selectivity in macaque V1: diversity  
926 and laminar dependence. *J. Neurosci.*, 22(13):5639–5651, July 2002.
- 927 35. R L De Valois, E W Yund, and N Hepler. The orientation and direction selectivity of cells in macaque visual  
928 cortex. *Vision Res.*, 22(5):531–544, 1982.
- 929 36. R L De Valois, D G Albrecht, and L G Thorell. Spatial frequency selectivity of cells in macaque visual cortex.  
930 *Vision Res.*, 22(5):545–559, 1982.
- 931 37. S Zeki. Colour coding in the cerebral cortex: the reaction of cells in monkey visual cortex to wavelengths and  
932 colours. *Neuroscience*, 9(4):741–765, August 1983.
- 933 38. M S Livingstone and D H Hubel. Anatomy and physiology of a color system in the primate visual cortex. *J.  
934 Neurosci.*, 4(1):309–356, January 1984.

- 935 39. G G Blasdel and G Salama. Voltage-sensitive dyes reveal a modular organization in monkey striate cortex.  
936 *Nature*, 321(6070):579–585, 1986.
- 937 40. A Grinvald, E Lieke, R D Frostig, C D Gilbert, and T N Wiesel. Functional architecture of cortex revealed by  
938 optical imaging of intrinsic signals. *Nature*, 324(6095):361–364, 1986.
- 939 41. Tobias Bonhoeffer and Amiram Grinvald. Iso-orientation domains in cat visual cortex are arranged in  
940 pinwheel-like patterns. *Nature*, 353(6343):429–431, 1991.
- 941 42. M Hübener, D Shoham, A Grinvald, and T Bonhoeffer. Spatial relationships among three columnar systems  
942 in cat area 17. *J. Neurosci.*, 17(23):9270–9284, December 1997.
- 943 43. Ian Nauhaus, Kristina J Nielsen, Anita A Disney, and Edward M Callaway. Orthogonal micro-organization  
944 of orientation and spatial frequency in primate primary visual cortex. *Nat. Neurosci.*, 15(12):1683–1690,  
945 December 2012.
- 946 44. Shu-Chen Guan, Nian-Sheng Ju, Louis Tao, Shi-Ming Tang, and Cong Yu. Functional organization of spatial  
947 frequency tuning in macaque V1 revealed with two-photon calcium imaging. *Prog. Neurobiol.*, 205:102120,  
948 October 2021.
- 949 45. R Desimone, T D Albright, C G Gross, and C Bruce. Stimulus-selective properties of inferior temporal neurons  
950 in the macaque. *J. Neurosci.*, 4(8):2051–2062, August 1984.
- 951 46. C G Gross, C E Rocha-Miranda, and D B Bender. Visual properties of neurons in inferotemporal cortex of the  
952 Macaque. *J. Neurophysiol.*, 35(1):96–111, January 1972.
- 953 47. Mark A Pinsk, Kevin DeSimone, Tirin Moore, Charles G Gross, and Sabine Kastner. Representations of faces  
954 and body parts in macaque temporal cortex: a functional MRI study. *Proc. Natl. Acad. Sci. U. S. A.*, 102(19):  
955 6996–7001, May 2005.
- 956 48. Doris Y Tsao, Winrich A Freiwald, Roger B H Tootell, and Margaret S Livingstone. A Cortical Region Consisting  
957 Entirely of Face-Selective Cells. *Science*, 311(5761):670–674, February 2006.
- 958 49. Mark A Pinsk, Michael Arcaro, Kevin S Weiner, Jan F Kalkus, Souheil J Inati, Charles G Gross, and Sabine  
959 Kastner. Neural representations of faces and body parts in macaque and human cortex: a comparative fMRI  
960 study. *J. Neurophysiol.*, 101(5):2581–2600, May 2009.
- 961 50. N Kanwisher, J McDermott, and M M Chun. The fusiform face area: a module in human extrastriate cortex  
962 specialized for face perception. *J. Neurosci.*, 17(11):4302–4311, June 1997.
- 963 51. R Epstein and N Kanwisher. A cortical representation of the local visual environment. *Nature*, 392(6676):  
964 598–601, April 1998.
- 965 52. P E Downing, Y Jiang, M Shuman, and N Kanwisher. A cortical area selective for visual processing of the  
966 human body. *Science*, 293(5539):2470–2473, September 2001.
- 967 53. Bruce D McCandliss, Laurent Cohen, and Stanislas Dehaene. The visual word form area: expertise for reading  
968 in the fusiform gyrus. *Trends Cogn. Sci.*, 7(7):293–299, July 2003.
- 969 54. Tanya Orlov, Tamar R Makin, and Ehud Zohary. Topographic representation of the human body in the  
970 occipitotemporal cortex. *Neuron*, 68(3):586–600, November 2010.
- 971 55. Kevin S Weiner and Kalanit Grill-Spector. Not one extrastriate body area: using anatomical landmarks,  
972 hMT+, and visual field maps to parcellate limb-selective activations in human lateral occipitotemporal cortex.  
973 *Neuroimage*, 56(4):2183–2199, June 2011.
- 974 56. Kalanit Grill-Spector and Kevin S Weiner. The functional architecture of the ventral temporal cortex and its role  
975 in categorization. *Nat. Rev. Neurosci.*, 15(8):536–548, August 2014.
- 976 57. Blake A Richards, Timothy P Lillicrap, Philippe Beaudoin, Yoshua Bengio, Rafal Bogacz, Amelia Christensen,  
977 Claudia Clopath, Rui Ponte Costa, Archy de Berker, Surya Ganguli, Colleen J Gillon, Danijar Hafner,  
978 Adam Kepecs, Nikolaus Kriegeskorte, Peter Latham, Grace W Lindsay, Kenneth D Miller, Richard Naud,  
979 Christopher C Pack, Panayiota Poirazi, Pieter Roelfsema, João Sacramento, Andrew Saxe, Benjamin Scellier,  
980 Anna C Schapiro, Walter Senn, Greg Wayne, Daniel Yamins, Friedemann Zenke, Joel Zylberberg, Denis  
981 Therien, and Konrad P Kording. A deep learning framework for neuroscience. *Nat. Neurosci.*, 22(11):  
982 1761–1770, November 2019.

- 983 58. Daniel L K Yamins and James J DiCarlo. Using goal-driven deep learning models to understand sensory  
984 cortex. *Nat. Neurosci.*, 19(3):356–365, 2016.
- 985 59. Kaiming He, Xiangyu Zhang, Shaoqing Ren, and Jian Sun. Deep residual learning for image recognition. In  
986 *Proceedings of the IEEE conference on computer vision and pattern recognition*, pages 770–778, 2016.
- 987 60. Michael J Arcaro and Margaret S Livingstone. A hierarchical, retinotopic proto-organization of the primate  
988 visual system at birth. *Elife*, 6, July 2017.
- 989 61. Chengxu Zhuang, Siming Yan, Aran Nayebi, Martin Schrimpf, Michael C Frank, James J DiCarlo, and Daniel  
990 L K Yamins. Unsupervised neural network models of the ventral visual stream. *Proc. Natl. Acad. Sci. U. S. A.*,  
991 118(3), January 2021.
- 992 62. Talia Konkle and George A Alvarez. A self-supervised domain-general learning framework for human ventral  
993 stream representation. *Nat. Commun.*, 13(1):491, January 2022.
- 994 63. Ting Chen, Simon Kornblith, Mohammad Norouzi, and Geoffrey Hinton. A Simple Framework for Contrastive  
995 Learning of Visual Representations. February 2020.
- 996 64. J Deng, W Dong, R Socher, L J Li, Kai Li, and Li Fei-Fei. ImageNet: A large-scale hierarchical image database.  
997 In *2009 IEEE Conference on Computer Vision and Pattern Recognition*, pages 248–255, June 2009.
- 998 65. Soumya Chatterjee, Kenichi Ohki, and R Clay Reid. Chromatic micromaps in primary visual cortex. *Nat.*  
999 *Commun.*, 12(1):2315, April 2021.
- 1000 66. Matthias Kaschube, Michael Schnabel, Siegrid Löwel, David M Coppola, Leonard E White, and Fred Wolf.  
1001 Universality in the evolution of orientation columns in the visual cortex. *Science*, 330(6007):1113–1116,  
1002 November 2010.
- 1003 67. Margaret Henderson and John T Serences. Biased orientation representations can be explained by experience  
1004 with nonuniform training set statistics. *J. Vis.*, 21(8):10, August 2021.
- 1005 68. Jeremy T Chang, David Whitney, and David Fitzpatrick. Experience-Dependent Reorganization Drives  
1006 Development of a Binocularly Unified Cortical Representation of Orientation. *Neuron*, May 2020.
- 1007 69. Dardo N Ferreiro, Sergio A Conde-Ocazonez, João H N Patriota, Luã C Souza, Moacir F Oliveira, Fred Wolf,  
1008 and Kerstin E Schmidt. Spatial clustering of orientation preference in primary visual cortex of the large rodent  
1009 agouti. *iScience*, 24(1):101882, January 2021.
- 1010 70. Dario L Ringach, Patrick J Mineault, Elaine Tring, Nicholas D Olivas, Pablo Garcia-Junco-Clemente, and  
1011 Joshua T Trachtenberg. Spatial clustering of tuning in mouse primary visual cortex. *Nat. Commun.*, 7:12270,  
1012 August 2016.
- 1013 71. Anupam K Garg, Peichao Li, Mohammad S Rashid, and Edward M Callaway. Color and orientation are jointly  
1014 coded and spatially organized in primate primary visual cortex, 2019.
- 1015 72. Nikolaus Kriegeskorte, Marieke Mur, and Peter Bandettini. Representational similarity analysis - connecting  
1016 the branches of systems neuroscience. *Front. Syst. Neurosci.*, 2(November):4, 2008.
- 1017 73. Eshed Margalit, Keith W Jamison, Kevin S Weiner, Luca Vizioli, Ru-Yuan Zhang, Kendrick N Kay, and  
1018 Kalanit Grill-Spector. Ultra-high-resolution fMRI of Human Ventral Temporal Cortex Reveals Differential  
1019 Representation of Categories and Domains, 2020.
- 1020 74. J V Haxby, M I Gobbini, M L Furey, A Ishai, J L Schouten, and P Pietrini. Distributed and overlapping  
1021 representations of faces and objects in ventral temporal cortex. *Science*, 293(5539):2425–2430, September  
1022 2001.
- 1023 75. Emily J Allen, Ghislain St-Yves, Yihan Wu, Jesse L Breedlove, Jacob S Prince, Logan T Dowdle, Matthias  
1024 Nau, Brad Caron, Franco Pestilli, Ian Charest, J Benjamin Hutchinson, Thomas Naselaris, and Kendrick Kay.  
1025 A massive 7T fMRI dataset to bridge cognitive neuroscience and artificial intelligence. *Nat. Neurosci.*, 25(1):  
1026 116–126, January 2022.
- 1027 76. Anthony Stigliani, Kevin S Weiner, and Kalanit Grill-Spector. Temporal Processing Capacity in High-Level  
1028 Visual Cortex Is Domain Specific. *J. Neurosci.*, 35(36):12412–12424, September 2015.

- 1029 77. Kevin S Weiner and Kalanit Grill-Spector. Sparsely-distributed organization of face and limb activations in  
1030 human ventral temporal cortex. *Neuroimage*, 52(4):1559–1573, 2010.
- 1031 78. Hyodong Lee, Eshed Margalit, Kamila M Jozwik, Michael A Cohen, Nancy Kanwisher, Daniel L K Yamins, and  
1032 James J DiCarlo. Topographic deep artificial neural networks reproduce the hallmarks of the primate inferior  
1033 temporal cortex face processing network. July 2020.
- 1034 79. Johannes Mehrer, Courtney J Spoerer, Emer C Jones, Nikolaus Kriegeskorte, and Tim C Kietzmann. An  
1035 ecologically motivated image dataset for deep learning yields better models of human vision. *Proc. Natl.  
1036 Acad. Sci. U. S. A.*, 118(8), February 2021.
- 1037 80. Maxime Oquab, Timothée Darcet, Théo Moutakanni, Huy Vo, Marc Szafraniec, Vasil Khalidov, Pierre  
1038 Fernandez, Daniel Haziza, Francisco Massa, Alaaeldin El-Nouby, Mahmoud Assran, Nicolas Ballas, Wojciech  
1039 Galuba, Russell Howes, Po-Yao Huang, Shang-Wen Li, Ishan Misra, Michael Rabbat, Vasu Sharma, Gabriel  
1040 Synnaeve, Hu Xu, Hervé Jegou, Julien Mairal, Patrick Labatut, Armand Joulin, and Piotr Bojanowski. DINOv2:  
1041 Learning Robust Visual Features without Supervision. April 2023.
- 1042 81. U Guclu and M A J van Gerven. Deep Neural Networks Reveal a Gradient in the Complexity of Neural  
1043 Representations across the Ventral Stream, 2015.
- 1044 82. Nathan C L Kong, Eshed Margalit, Justin L Gardner, and Anthony M Norcia. Increasing neural network  
1045 robustness improves match to macaque V1 eigenspectrum, spatial frequency preference and predictivity.  
1046 *PLoS Comput. Biol.*, 18(1):e1009739, January 2022.
- 1047 83. Eric Elmoznino and Michael F Bonner. High-performing neural network models of visual cortex benefit from  
1048 high latent dimensionality. February 2023.
- 1049 84. Marco Del Giudice. Effective Dimensionality: A Tutorial. *Multivariate Behav. Res.*, 56(3):527–542, 2021.
- 1050 85. Carsen Stringer, Marius Pachitariu, Nicholas Steinmetz, Matteo Carandini, and Kenneth D Harris.  
1051 High-dimensional geometry of population responses in visual cortex. *Nature*, 571(7765):361–365, July 2019.
- 1052 86. Dmitri B Chklovskii, Thomas Schikorski, and Charles F Stevens. Wiring optimization in cortical circuits.  
1053 *Neuron*, 34(3):341–347, 2002.
- 1054 87. Sebastian Moeller, Winrich A Freiwald, and Doris Y Tsao. Patches with links: a unified system for processing  
1055 faces in the macaque temporal lobe. *Science*, 320(5881):1355–1359, June 2008.
- 1056 88. Michael S Beauchamp, Denise Oswald, Ping Sun, Brett L Foster, John F Magnotti, Soroush Niketeghad, Nader  
1057 Pouratian, William H Bosking, and Daniel Yoshor. Dynamic Stimulation of Visual Cortex Produces Form Vision  
1058 in Sighted and Blind Humans. *Cell*, 181(4):774–783.e5, May 2020.
- 1059 89. Maureen van der Grinten, Jaap de Ruyter van Steveninck, Antonio Lozano, Laura Pijnacker, Bodo Rückauer,  
1060 Pieter Roelfsema, Marcel van Gerven, Richard van Wezel, Umut Güçlü, and Yağmur Güçlütürk. Biologically  
1061 plausible phosphene simulation for the differentiable optimization of visual cortical prostheses. December  
1062 2022.
- 1063 90. Jacob Granley, Alexander Riedel, and Michael Beyeler. Adapting Brain-Like Neural Networks for Modeling  
1064 Cortical Visual Prostheses. September 2022.
- 1065 91. Elia Shahbazi, Timothy Ma, Martin Pernus, Walter J Scheirer, and Arash Afraz. The causal role of the inferior  
1066 temporal cortex in visual perception. January 2023.
- 1067 92. Katharina Dobs, Julio Martinez, Alexander J E Kell, and Nancy Kanwisher. Brain-like functional specialization  
1068 emerges spontaneously in deep neural networks. *Science Advances*, 8(11):eabl8913, 2022.
- 1069 93. Sam V Norman-Haignere, Jenelle Feather, Dana Boebinger, Peter Brunner, Anthony Ritaccio, Josh H  
1070 McDermott, Gerwin Schalk, and Nancy Kanwisher. A neural population selective for song in human auditory  
1071 cortex. *Curr. Biol.*, 32(7):1470–1484.e12, April 2022.
- 1072 94. Rosemary A Cowell and Garrison W Cottrell. What evidence supports special processing for faces? A  
1073 cautionary tale for fMRI interpretation. *J. Cogn. Neurosci.*, 25(11):1777–1793, November 2013.
- 1074 95. Lukas Vogelsang, Sharon Gilad-Gutnick, Evan Ehrenberg, Albert Yonas, Sidney Diamond, Richard Held,  
1075 and Pawan Sinha. Potential downside of high initial visual acuity. *Proc. Natl. Acad. Sci. U. S. A.*, 115(44):  
1076 11333–11338, October 2018.

- 1077 96. Omisa Jinsi, Margaret M Henderson, and Michael J Tarr. Early experience with low-pass filtered images  
1078 facilitates visual category learning in a neural network model. *PLoS One*, 18(1):e0280145, January 2023.
- 1079 97. A Nayebi, J Sagastuy-Brena, D M Bear, K Kar, J Kubilius, S Ganguli, D Sussillo, J J DiCarlo, and D L K Yamins.  
1080 Recurrent Connections in the Primate Ventral Visual Stream Mediate a Tradeoff Between Task Performance  
1081 and Network Size During Core Object Recognition. *Neural Computation*, 34(8):1652–1675, July 2022.
- 1082 98. Jianhua Cang, Megumi Kaneko, Jena Yamada, Georgia Woods, Michael P Stryker, and David A Feldheim.  
1083 Ephrin-as guide the formation of functional maps in the visual cortex. *Neuron*, 48(4):577–589, November  
1084 2005.
- 1085 99. M Meister, R O Wong, D A Baylor, and C J Shatz. Synchronous bursts of action potentials in ganglion cells of  
1086 the developing mammalian retina. *Science*, 252(5008):939–943, May 1991.
- 1087 100. Jinwoo Kim, Min Song, Jaeson Jang, and Se-Bum Paik. Spontaneous Retinal Waves Can Generate  
1088 Long-Range Horizontal Connectivity in Visual Cortex. *J. Neurosci.*, 40(34):6584–6599, August 2020.
- 1089 101. Todd McLaughlin, Christine L Torborg, Marla B Feller, and Dennis D M O’Leary. Retinotopic map refinement  
1090 requires spontaneous retinal waves during a brief critical period of development. *Neuron*, 40(6):1147–1160,  
1091 December 2003.
- 1092 102. Xinxin Ge, Kathy Zhang, Alexandra Gribizis, Ali S Hamodi, Aude Martinez Sabino, and Michael C Crair. Retinal  
1093 waves prime visual motion detection by simulating future optic flow. *Science*, 373(6553), July 2021.
- 1094 103. Rishi Rajalingham and James J DiCarlo. Reversible Inactivation of Different Millimeter-Scale Regions of  
1095 Primate IT Results in Different Patterns of Core Object Recognition Deficits. *Neuron*, 102(2):493–505.e5,  
1096 April 2019.
- 1097 104. Tiago Marques, Martin Schrimpf, and James J DiCarlo. Multi-scale hierarchical neural network models that  
1098 bridge from single neurons in the primate primary visual cortex to object recognition behavior. March 2021.
- 1099 105. Santiago A Cadena, Konstantin F Willeke, Kelli Restivo, George Denfield, Fabian H Sinz, Matthias Bethge,  
1100 Andreas S Tolias, and Alexander S Ecker. Diverse task-driven modeling of macaque V4 reveals functional  
1101 specialization towards semantic tasks. May 2022.
- 1102 106. Pouya Bashivan, Kohitij Kar, and James J DiCarlo. Neural population control via deep image synthesis.  
1103 *Science*, 364(6439), May 2019.
- 1104 107. Priya Goyal, Quentin Duval, Jeremy Reizenstein, Matthew Leavitt, Min Xu, Benjamin Lefaudeux, Mannat  
1105 Singh, Vinicius Reis, Mathilde Caron, Piotr Bojanowski, and Others. *Vissl*, 2021.
- 1106 108. Ilya Loshchilov and Frank Hutter. SGDR: Stochastic Gradient Descent with Warm Restarts. August 2016.
- 1107 109. Noah C Benson, Jennifer M D Yoon, Dylan Forenzo, Stephen A Engel, Kendrick N Kay, and Jonathan Winawer.  
1108 Variability of the Surface Area of the V1, V2, and V3 Maps in a Large Sample of Human Observers. *J.*  
1109 *Neurosci.*, 42(46):8629–8646, November 2022.
- 1110 110. T Yoshioka, J B Levitt, and J S Lund. Intrinsic lattice connections of macaque monkey visual cortical area V4.  
1111 *J. Neurosci.*, 12(7):2785–2802, July 1992.
- 1112 111. Alex Krizhevsky, Geoffrey E Hinton, and Ilya Sutskever. ImageNet Classification with Deep Convolutional  
1113 Neural Networks. *the Neural Information Processing Systems Foundation 2012 conference*, pages 1–9, 2012.
- 1114 112. Giuseppe Vettigli. MiniSom: minimalistic and NumPy-based implementation of the Self Organizing Map, 2018.
- 1115 113. Lior Bugatus, Kevin S Weiner, and Kalanit Grill-Spector. Task alters category representations in prefrontal but  
1116 not high-level visual cortex. *Neuroimage*, 155:437–449, July 2017.
- 1117 114. James Munkres. Algorithms for the Assignment and Transportation Problems. *Journal of the Society for*  
1118 *Industrial and Applied Mathematics*, 5(1):32–38, March 1957.



## 1119 **Supplementary Information**

### 1120 **V1-like maps produced with alternative feature sets**

1121 Figure 2 demonstrates that co-training for spatial and task losses is sufficient to generate V1-like topography.  
1122 However, we have not ruled out the possibility that generating orientation-selective units and arranging them on  
1123 the cortical sheet via other strategies could produce V1-like maps. To address this concern, we derive orientation  
1124 preference maps (OPMs) from three different strategies for learning and spatially organizing model units. We first  
1125 compare the standard TDANN, in which unit positions are fixed prior to training and model weights are optimized to  
1126 minimize both task and spatial losses, to a Task Only DCNN whose weights are optimized only for the task loss. To  
1127 generate an OPM from the Task Only model, we freeze network weights then iteratively shuffle model units on the  
1128 cortical sheet such that the Spatial Loss is minimized post-hoc. Accordingly, we refer to this model as a "Post-hoc"  
1129 arrangement of DCNN features. We find that OPM smoothness is nearly identical when co-learning features with  
1130 the spatial loss (i.e., TDANN) than when first learning features and then post-hoc arranging units in the cortical sheet  
1131 (Supplementary Figure S4). A third alternative is to bypass the learning of features altogether and use a hard-coded  
1132 Gabor filterbank (GFB) to generate model units, as has been suggested as a model of V1 neuron tuning (e.g. Jones  
1133 and Palmer [5], Dapello et al. [3]). Following the same approach as in the Task Only model for deriving OPMs, we  
1134 find that the hard-coded GFB features fail to produce a smooth OPM. How can we reconcile the apparent inadequacy  
1135 of the Gabor filterbank in generating V1-like topography with its strong orientation selectivity? One possibility is that  
1136 a Gabor filterbank lacks the required complexity to form responses to natural images that drive brain-like topography,  
1137 but that simpler stimuli may improve the accuracy of its topographic predictions. To test whether the nature of the  
1138 images presented to the model matters, we evaluated the same three feature sets (TDANN, Post-hoc, Task Only,  
1139 and GFB) on a set of simple sine grating images (Figure S4a, bottom). Interestingly, we find that the TDANN,  
1140 Post-hoc Task Only, and GFB feature sets all produce smooth OPMs when their units are organized with respect  
1141 to correlations of sine grating responses. We conclude that the TDANN is the only model that, by co-learning  
1142 features and topography, is able to produce brain-like OPMs from realistically complex natural inputs. Task Only  
1143 and Hand-Crafted feature spaces are capable of producing V1-like OPMs only when presented with simple inputs,  
1144 whereas the core advantage of the TDANN is its ability to learn a feature space that produces brain-like functional  
1145 organization in the presence of realistically complex natural images.

### 1146 **Natural image inputs are required for the emergence of brain-like functional organization**

1147 Work in developmental neuroscience and psychology has called into consideration the influence of visual experience  
1148 on the development of structure and function in visual cortex. We leveraged the ability of self-supervised TDANNs  
1149 to predict functional organization after learning from unlabeled visual data streams to determine which inputs might  
1150 drive the emergence of brain-like topographic maps. We evaluated networks trained on four distinct image datasets,  
1151 including the natural image datasets ImageNet and Ecoset [9], and two artificial datasets: sine gratings and white  
1152 noise images. We find that for both natural image datasets, there is brain-like functional organization of V1-like  
1153 and VTC-like layers. In the V1-like layer, 14% of units in the Ecoset-trained network and 20% of units in the  
1154 ImageNet-trained network were strongly orientation selective (circular variance  $< 0.6$ ), and we observe smooth  
1155 OPMs with pinwheels in models trained from both datasets. Further, we found similar numbers of VTC-like layer  
1156 units with selectivity  $t > 5$  in both models (12.7% for Ecoset and 14.2% for ImageNet), and we detect patches  
1157 selective for all five categories in both models (Figure S9).

1158 While the suitability of naturalistic stimuli for generating brain-like functional organization may not be surprising, we  
1159 wanted to test if simpler artificial datasets could succeed in matching neural data for two reasons. First, it has  
1160 been demonstrated that patterned endogenous activity prior to eye opening can establish visual cortical circuitry [4].  
1161 Second, if artificial synthetic stimuli were suitable for constructing brain models, we could avoid needing to collect  
1162 large natural image datasets. We trained TDANN on two artificial stimulus sets: a set of sine grating stimuli that may  
1163 loosely mirror endogenous activity patterns, and Gaussian white noise images. The grating-trained model exhibited  
1164 a very high fraction of strongly orientation selective units in the V1-like layer (73%). However, the grating-trained  
1165 model had no category selectivity (1.2% of units selective at  $t > 5$ , averaged across categories), and no detectable  
1166 patches. Thus, simple oriented stimuli may be sufficient to drive V1-like map formation, but natural stimuli are  
1167 necessary to develop the remainder of the ventral visual pathway. We next evaluated a model trained on white noise,  
1168 which allows us to isolate the effects of the model architecture and loss functions in the absence of structure in the  
1169 input data. We find that training on white noise prevents the learning of strongly orientation-selective units in the  
1170 V1-like layer (0% of units with circular variance  $< 0.6$ ) or strongly category-selective units in the VTC-like layer (4%  
1171 of units with  $t > 5$ ). Surprisingly, however, the noise-trained TDANN does learn some weak functional organization.  
1172 In the V1-like layer, a weak orientation preference map is formed, and in the VTC-like layer, two character-selective  
1173 patches and one face-selective patch is observed. These results suggest that the spatial loss is able to produce some

1174 topographic structure even in the absence of patterned inputs, although the strength of the selectivity is extremely  
1175 weak. Taken together, these analyses of the impact of training data on functional organization support the necessity  
1176 and sufficiency of natural images for the emergence of robust V1-like and VTC-like topographic maps.

### 1177 **Probing the tuning of unit populations outside of category-selective patches**

1178 If the VTC-like layer smoothly encodes a space of objects, we might expect that images synthesized to drive high  
1179 responses in nearby regions of the cortical sheet would be perceptually similar. Indeed, we find that optimal image  
1180 characteristics smoothly vary across the cortical surface. Higher spatial frequency and rectilinear features dominate  
1181 the upper right sides of the map, while curvilinear and lower spatial frequency features best drive the top and bottom  
1182 edges. We find that these optimal images also align with category-selectivity, e.g., the input images that best drive  
1183 units in face-selective patches tend to contain eyes and fall in the more curvilinear regions of feature space. Images  
1184 synthesized to maximize regions that fall between patches (sites 5, 10, 11, 15, 16, and 20) lack clearly discernible  
1185 object categories, but nonetheless follow the smooth gradients of image features across the cortical surface. Thus,  
1186 it appears that the VTC-like layer learns a smooth mapping of object space in two dimensions, and that patches  
1187 emerge as regions of that space that align with the category localization stimuli that we use to probe the model.

### 1188 **Supplemental Methods**

1189 **Dimensionality Summarize by Power Law Exponent.** Following Kong et al. [7], Stringer et al. [11], we summarize the  
1190 eigenvalues by fitting a line to the log-log plot of eigenvalues against their principal component index, and report the  
1191 absolute value of the best fit line as the power law exponent. To prevent fitting to nonlinear regions in the earliest  
1192 and latest parts of the distribution, the line is fit from the 2nd to the 50th principal component.

1193 **Linear regression.** Neural predictivity is computed against a given dataset as the mean variance explained across  
1194 neurons and splits of the data. In practice we follow the parameters and design decisions made by the BrainScore  
1195 team [10]; they are repeated here for completeness. We use partial least squares (PLS) regression to predict the  
1196 activity of a given neuron as a linear weighted sum of model units in a given layer. Model activations are preprocessed  
1197 by first projecting unit responses to ImageNet images onto the first 1000 principal components, i.e. each component  
1198 is a linear mixture of model units. This projection is used when fitting on the stimuli that were shown to the animal.  
1199 When fitting V1, we use data from Cadena et al. [2], which consists of single-neuron recordings to a set of natural  
1200 images. When fitting V4 and IT, we use data from Majaj, Hong, et al., 2015 [8], which consists of multi-electrode  
1201 array data in responses to quasi-naturalistic scenes with a variety of objects on a variety of backgrounds. Variance  
1202 explained is corrected by dividing raw predictivity by the internal noise ceiling, a measure of the consistency of each  
1203 recorded neuron.

1204 **Unit Clustering.** The degree to which of responses to natural images are clustered is computed by considering the  
1205 locations of the 5% of units that respond most strongly to a given input image. We compute the distribution of  
1206 pairwise distances between these highly-active units, then count the number of pairs that are within 10.0mm of each  
1207 other: if the count is high, then the active units are concentrated into a small number of clusters. Finally, clusteriness  
1208 is defined as the ratio between the number of nearby pairs in the true response pattern to the number of nearby pairs  
1209 when locations are randomly shuffled. We compute results for 10 random position shuffles, 64 randomly-selected  
1210 images used as input, and five random initial seeds for each model.

1211 **Gabor Filter Bank (GFB).** In Figure S4, we generate responses from a Gabor filter bank by following the VOneNet  
1212 implementation in Dapello et al. [3]. For computational tractability and to produce a similar quantity of units as in the  
1213 TDANN V1-like layer, we reduce the number of simple and complex channels from 256 to 64 each, and increase the  
1214 stride of the convolution from 4 to 8 pixels. The resulting filter bank is then treated identically to the TDANN V1-like  
1215 layer when extracting responses and constructing tuning curves.

1216 The orientation preference map (OPM) for the GFB model is produced by assigning GFB outputs to random initial  
1217 positions, then minimizing the Spatial Loss by iteratively swapping the locations of randomly-selected pairs of units  
1218 as described above.

1219 **Stimulus Optimization.** We use image synthesis methods, implemented in the *lucent* Python package ([https://](https://github.com/greentfrapp/lucent)  
1220 [github.com/greentfrapp/lucent](https://github.com/greentfrapp/lucent)), to generate images which reproduce patterns of stimulation. Specifically, we  
1221 synthesize an input image that minimizes the mean squared error between a desired pattern of activity and the actual  
1222 pattern obtained by presenting the synthesized image to the network. The desired pattern of activity is set according  
1223 to a two-dimensional Gaussian centered over some region of the cortical sheet. In these experiments we set the  
1224  $\sigma$  parameter of the Gaussian to 3.5mm. For efficiency, we also remove units far from the center of the Gaussian  
1225 from the computation of the mean squared error: units below 10% of the height of the Gaussian are ignored. All

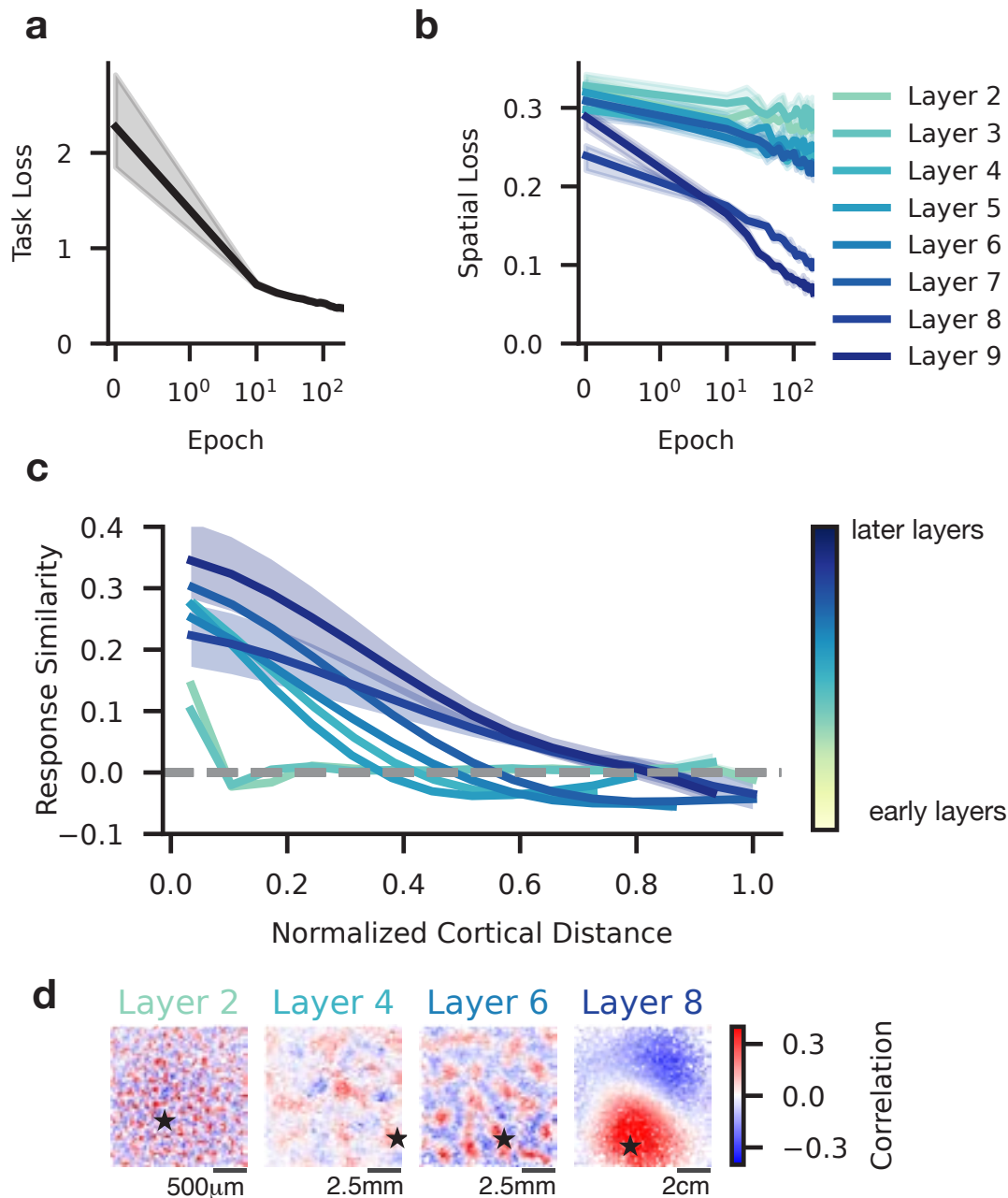


**Figure S1. Minimization of loss components during training.** (a) Task loss throughout training. (b) Spatial loss in each of the eight convolutional layers during training. Shaded area: 95% confidence interval (CI) across random initializations. (c) Response correlation decreases as a function of the cortical distance between model unit pairs in each model layer. Shaded region: 95% CI from repeated sampling of different cortical neighborhoods in each layer. (d) Portions of the cortical sheet from each of four convolutional layers; units colored according to their correlation with an arbitrarily selected seed unit, marked by the black star.

1226 synthesized images begin as 128 x 128 pixels of white noise and are optimized for 1,024 steps. We retain the default  
 1227 settings for image transforms, which include optimization in the Fourier basis, color channel decorrelation, jittering,  
 1228 rotation, and padding.

1229 **Retinal Waves.** In Figure S18 we organize DCNN units in the cortical sheet according to their response correlations  
 1230 to a series of simulated retinal waves.

1231 **Creating Retinal Waves** Our simulation of retinal wave activity is heavily inspired by the description in Kim et al.  
 1232 [6]. We simulate the retina as a two-dimensional circle of radius 320px. The retina has three spatially-overlapping  
 1233 cell layers: one for ON-RGCs (retinal ganglion cells), one for OFF-RGCs, and one for amacrine cells. Each cell can

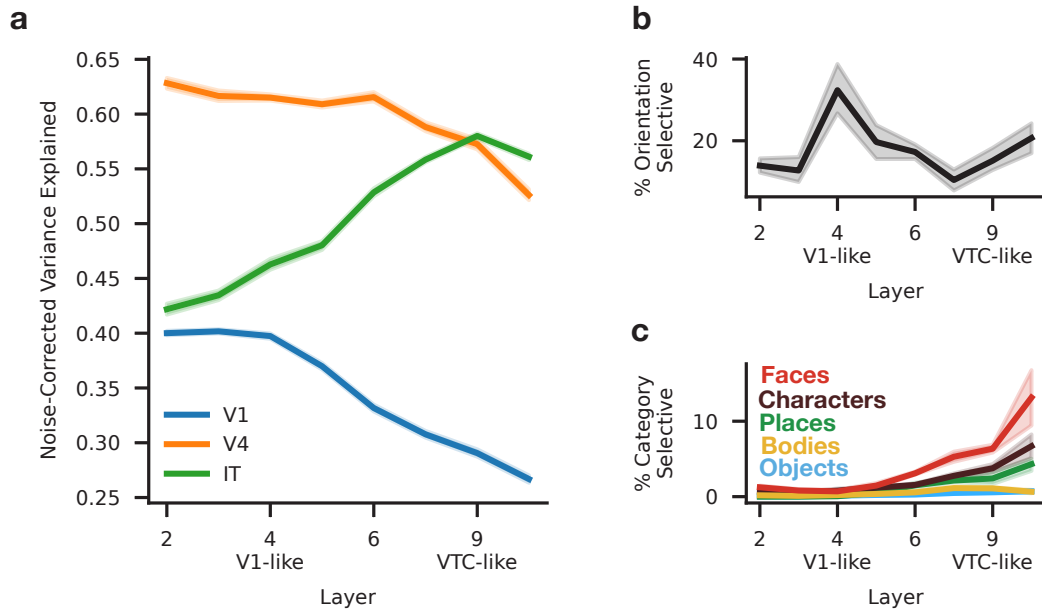


**Figure S2. Selection of V1-like and VTC-like layers.** (a) Variance explained by linear regression of TDANN layer outputs to measurements in macaque V1, V4, and IT. V1 predictivity peaks in the first three layers, whereas IT predictivity peaks in the last two layers. (b) Fraction of units strongly orientation selective in each layer. (c) Fraction of units that are strongly selective for each category ( $t$ -value  $> 10$ ) in each layer.

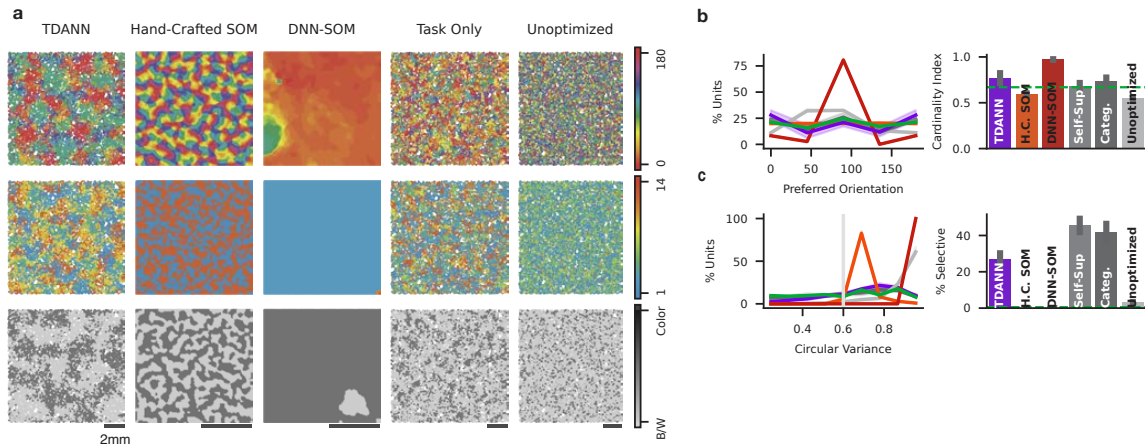


**Figure S3. Topographic and representational benchmarks in the V1-like model layer** (a) Orientation, spatial frequency, and chromatic preference maps for all candidate model types. (b) Left: Distribution of preferred orientations for each model type. Right: Cardinality index, computed as the fraction of units selective for cardinal orientations to units selective for the obliques. Dashed green light indicates value in macaque V1. (c) Left: Distribution of circular variance for each model and for macaque V1. Vertical line indicates cutoff for strong selectivity. Right: percentage of units strongly selective for orientations in each model type.

1234 be in one of four states: inhibited, recruitable (but not currently active), refractory (recently active but not recruitable  
 1235 yet), or active (currently "on"). Cells are connected to each other according to the following rules: 1) ON-RGCs are  
 1236 connected to one another in an excitatory fashion within a radius of  $r_{ON}$ , 2) ON-RGCs are connected to amacrine  
 1237 cells in an excitatory fashion within a radius of  $r_{ON}$ , and amacrine cells inhibit OFF-RGCs within a radius of  $r_{amacrine}$ .

1238 A wave is initiated by setting some subset of the ON-RGCs to the "active" state. The activated subset is determined  
 1239 by picking a random location along the edge of the retina and activating cells along a thin strip at that location. The  
 1240 wave is then propagated for up to  $t$  timesteps (propagation is halted if the wave runs off screen and all cells are  
 1241 off). At each timestep, activity is propagated as follows. First, all cells that have been active longer than a specified

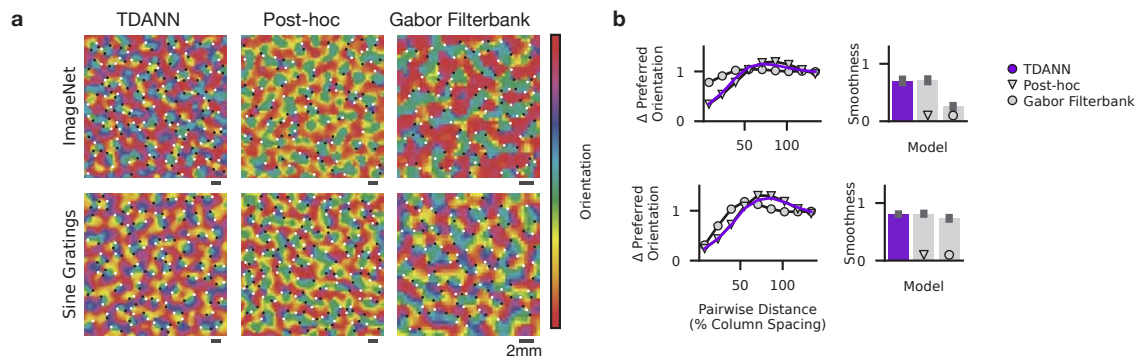


**Figure S4. Smoothed OPMs from alternative feature spaces** (a) Top row: smoothed OPMs from the TDANN, a Task Only model with post-hoc unit organization, and a Gabor Filterbank with post-hoc unit organization, where units are brought closer together if they have similar responses to ImageNet images. Bottom row: same as top, but with unit proximity optimized with respect to sine grating image responses. (b) Pairwise orientation tuning difference over distance, and corresponding smoothness scores, for the maps in (a).

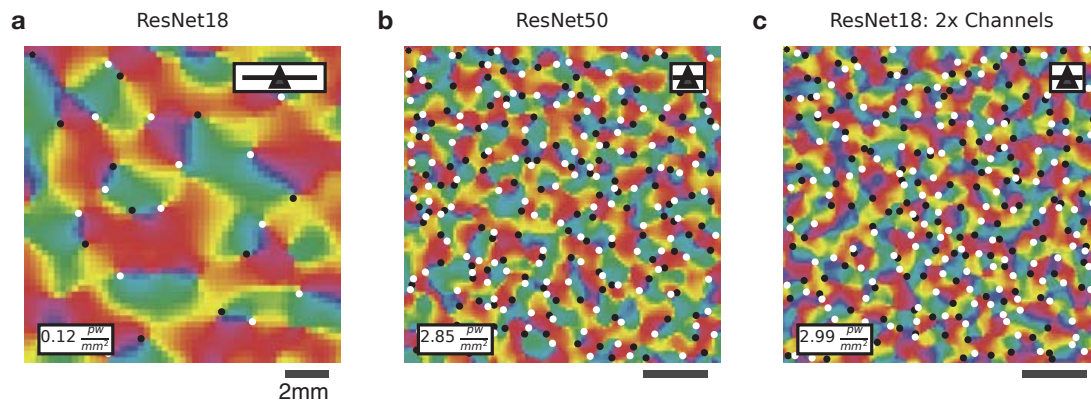


**Figure S5. Orientation preference maps (OPMs) and pinwheel density in alternative models** For demonstration, all models in this figure had unit positions organized post-hoc to achieve a strong OPM, i.e., they are not proper TDANNs. (a) OPM in a small region of the standard ResNet-18 TDANN. Pinwheels are shown by black and white dots. (b) OPM in the V1-like layer of a categorization-trained ResNet-50, in which the increased number of channels allows a reduction of cortical neighborhood size and, accordingly, a dramatic increase in pinwheel density. (c) OPM in the V1-like layer of a categorization-trained ResNet-18 with twice the number of channels in each layer, in which the increased number of channels allows a reduction of cortical neighborhood size and, accordingly, a dramatic increase in pinwheel density.

1242 "active duration" are set to the refractory state. Second, cell activity levels are updated by multiplying the connectivity  
 1243 matrices with the previous activity states. Third, we activate all ON-RGCs who are in the recruitable state and whose  
 1244 activity exceeds an activity threshold of  $t_{ON-active}$ . Fourth, we inhibit all OFF-RGCs whose activity falls below a  
 1245 threshold of  $t_{OFF-active}$ . OFF-RGCs whose activity passes that threshold are activated if they are currently in the  
 1246 recruitable state. Finally, amacrine cells whose activity exceeds  $t_{amacrine-active}$  are set to active. The remainder of  
 1247 the amacrine cells are made recruitable instead. Images of the simulated activity at each stage are produced by  
 1248 creating binary masks of the locations of active ON-RGCs. Half of the waves are randomly assigned to map the  
 1249 binary images to a black and white colormap, and the remainder are assigned to a red and green colormap.

1250 In this work, we produce retinal waves with two sets of parameters. The following parameters are common to both  
 1251 sets of retinal waves:  $r_{on} = 15$ ,  $r_{amacrine} = 1.5$ ,  $t = 20$ ,  $t_{ON-active} = 7$ ,  $t_{amacrine-active} = 0.1$ ,  $t_{OFF-active} = 0.1$ . In  
 1252 one of the two sets of waves, the active duration is set to 100ms, and in the other, the active duration is set to 200ms.  
 1253 In practice, the waves produced with the longer active duration are twice as thick.

1254 **Measuring Responses to Waves** Each wave consists of a number of images, one per timestep of the simulation.  
 1255 Because the simulated retina is circular, the corners of each image never contain simulated activity. To make better  
 1256 use of each image, we take a central square crop of each image of size  $M \times M$  pixels then resize the image back  
 1257 to  $224 \times 224$  pixels.  $M$  is selected such that all regions of the crop contain activity: for an image of size  $224px$ ,

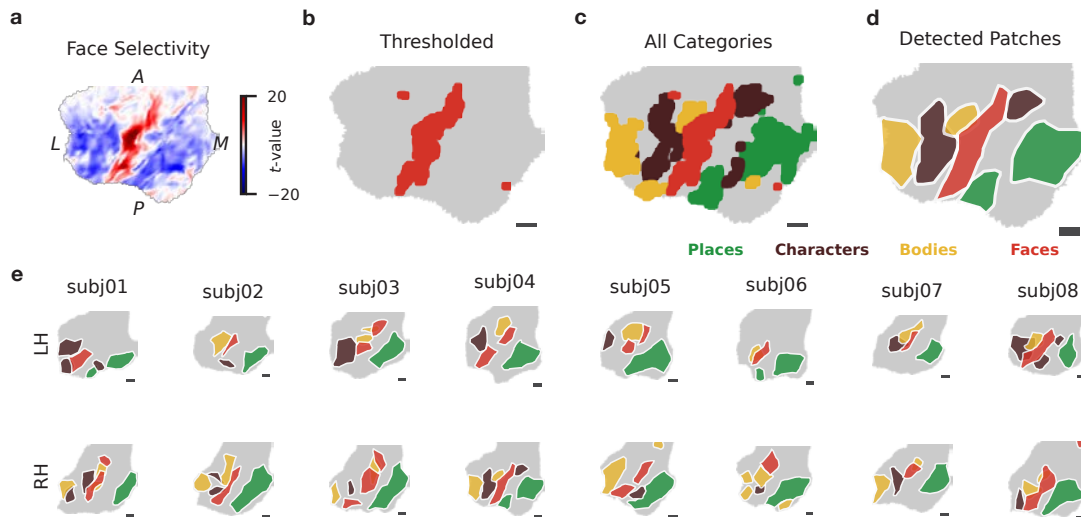


**Figure S6. Data in each human subject from the NSD fLoc experiment and patch detection protocol** All scale bars: 2mm. **(a)** Map of face selectivity in the right-hemisphere VTC region of interest (ROI) for one example subject. A: anterior, M: medial, L: lateral, P: posterior. **(b)** Thresholded face selectivity map for the same subject as (a). **(c)** Category selectivity map for all five fLoc categories. **(d)** Patches detected from the category selective clusters in (c). **(e)** Detected patches in each hemisphere (LH = left hemisphere, RH = right hemisphere) for each subject.

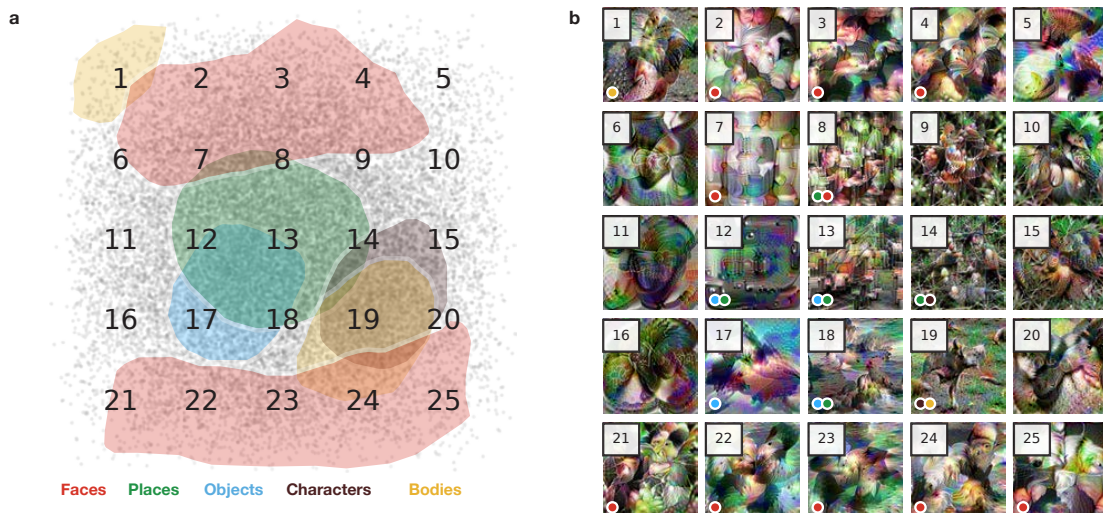


**Figure S7. Optimal stimuli throughout the VTC-like layer** **(a)** VTC-like layer of an example TDANN model. Overlaid numbers correspond to sub-panels in (b). **(b)** Images synthesized to maximally activate a local population of units centered at the indicated location in (a). Small dot in bottom left of each image indicates the patch membership of that location, e.g., a red dot indicates that the image optimally drives units that happen to be in a face-selective patch.

1258  $M = \sqrt{2 \times \left(\frac{224}{2}\right)^2} \approx 158$ . As with all other images presented to the DCNN models, the images are then preprocessed  
1259 and normalized.

1260 For a wave with  $t$  timesteps, each model unit produces  $t$  responses. We integrate responses to each wave by  
1261 computing the mean response across all waves. Anecdotally, similar results are achieved by computing the maximum  
1262 response instead of the mean. Unit-to-unit correlations are then computed by considering the vector of integrated  
1263 responses for each wave. We use the unit-to-unit correlations to perform swap-based organization of units on the  
1264 cortical surface such that correlated units are moved to be nearby one another.

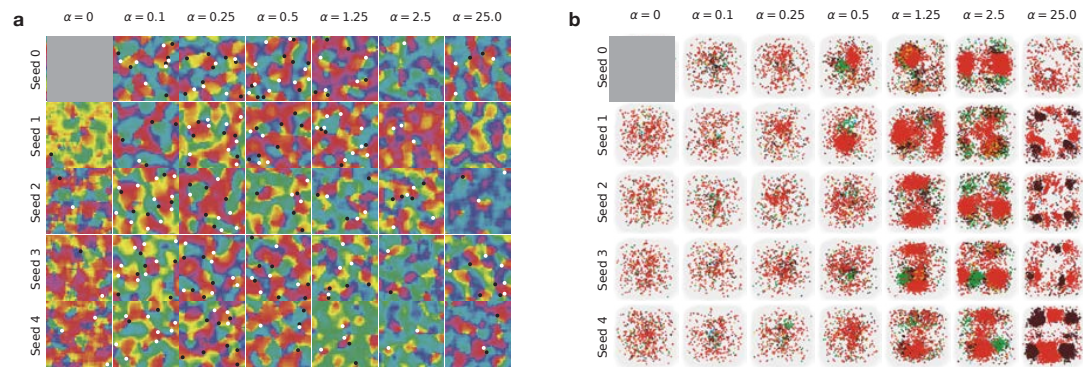


**Figure S8. Topographic maps for models trained with the Relative SL and the Supervised Categorization objective (a)** Orientation preference maps (OPMs) in the V1-like layer of models at each level of  $\alpha$  trained from five different random seeds with the categorization objective. A region of each cortical sheet is shown, with black and white dots indicating locations of detected clockwise and counter-clockwise pinwheels, respectively. Gray square covers the Task Only seed 0, which was used during position initialization. **(b)** Category selectivity maps for the VTC-like layer of each model in (A). Plotting conventions as in Figure 3.

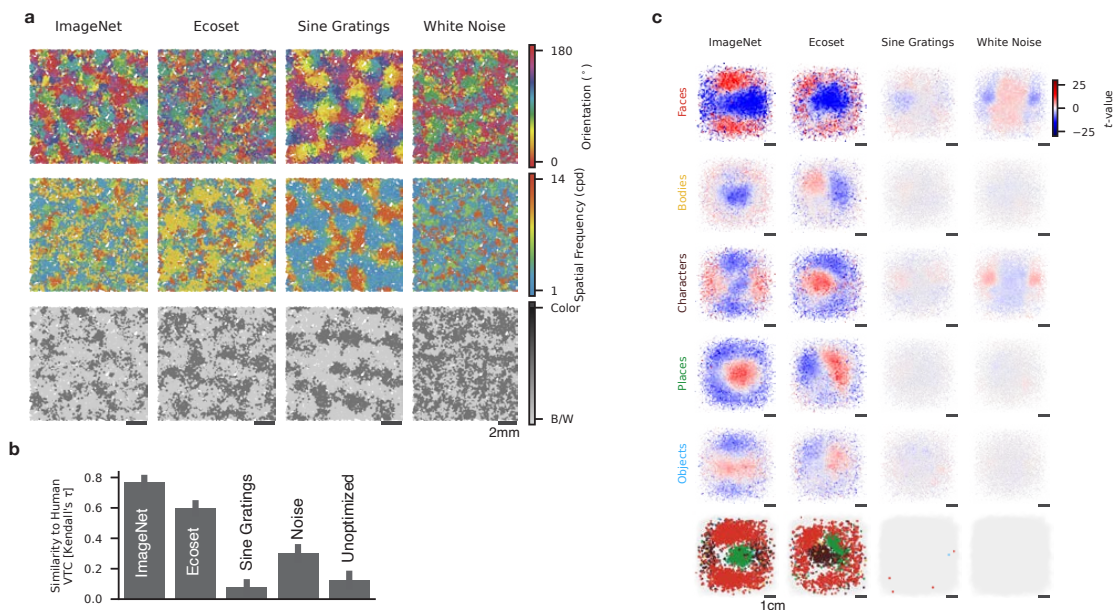


**Figure S9. Topographic maps from models trained with different training datasets (a)** Orientation, spatial frequency, and chromatic preference maps in the V1-like layer of models trained with ImageNet images, the *Ecoset* training set, a set of hand-selected sine gratings (increased  $\alpha = 10$ ), and Gaussian white noise images. **(b)** Representational similarity between human VTC and models trained with each dataset. Error bar: 95% CI across human hemispheres. **(c)** Category selectivity maps for the VTC-like layer of each model in (a). Plotting conventions as in Figure 3.

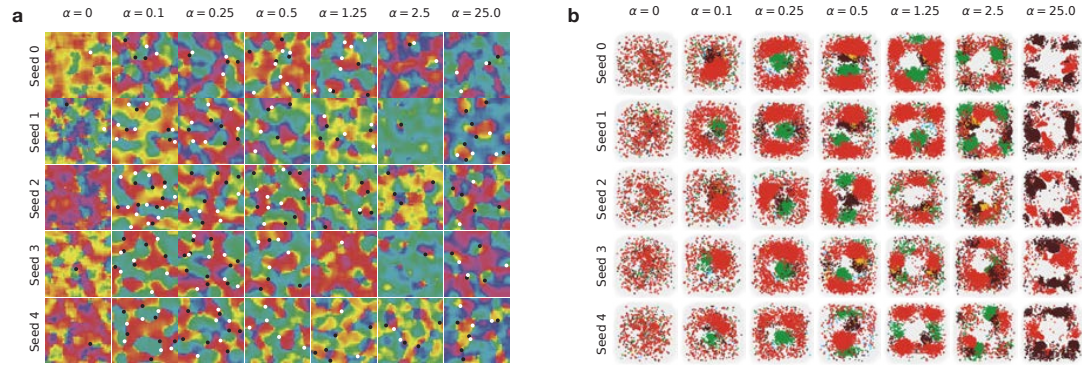


**Figure S10. Topographic maps for models trained with the Relative SL and self-supervision** (a) Orientation preference maps (OPMs) in the V1-like layer of models at each level of  $\alpha$  trained from five different random seeds with the Relative Spatial Loss (SL). A region of each cortical sheet is shown, with black and white dots indicating locations of detected clockwise and counter-clockwise pinwheels, respectively. (b) Category selectivity maps for the VTC-like layer of each model in (a). Plotting conventions as in Figure 3.

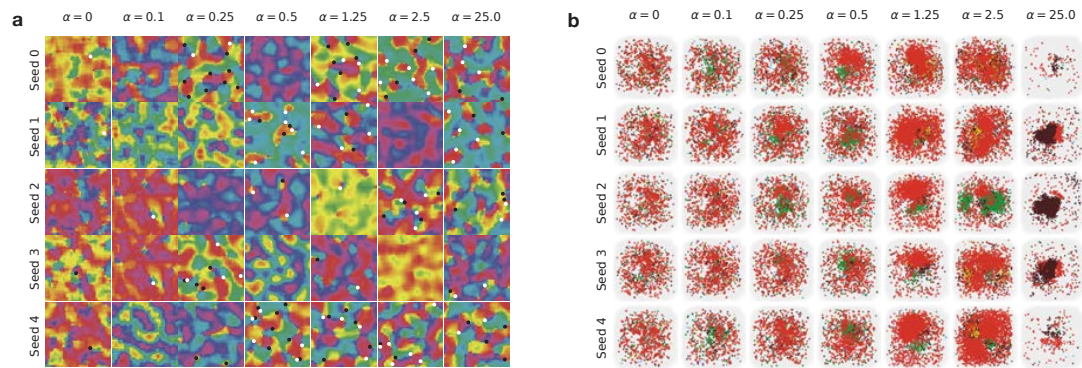


**Figure S11. Topographic maps for models trained with the Absolute SL** (a) Orientation preference maps (OPMs) in the V1-like layer of models at each level of  $\alpha$  trained from five different random seeds with the Absolute Spatial Loss (SL). A mm region of each cortical sheet is shown, with black and white dots indicating locations of detected clockwise and counter-clockwise pinwheels, respectively. (b) Category selectivity maps for the VTC-like layer of each model in (a). Plotting conventions as in Figure 3.

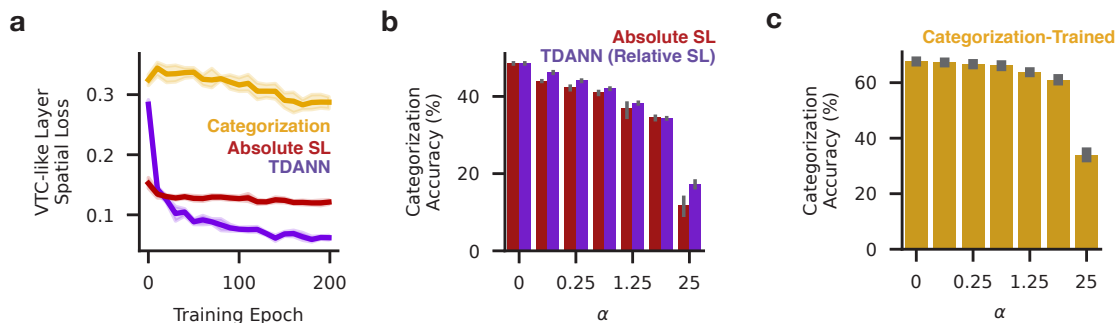


**Figure S12. Additional comparison of models trained with different task and spatial objectives** (a) Spatial loss in the VTC-like layer of TDANN models (purple), categorization-trained models (gold), and models trained with the Absolute SL (red) throughout training. (b) Categorization accuracy (top-1 ImageNet validation set performance) for models trained at each level of  $\alpha$  with either the Relative (purple) or Absolute (red) SL. (c) Categorization accuracy for models trained at each level of  $\alpha$  directly on the supervised categorization objective.



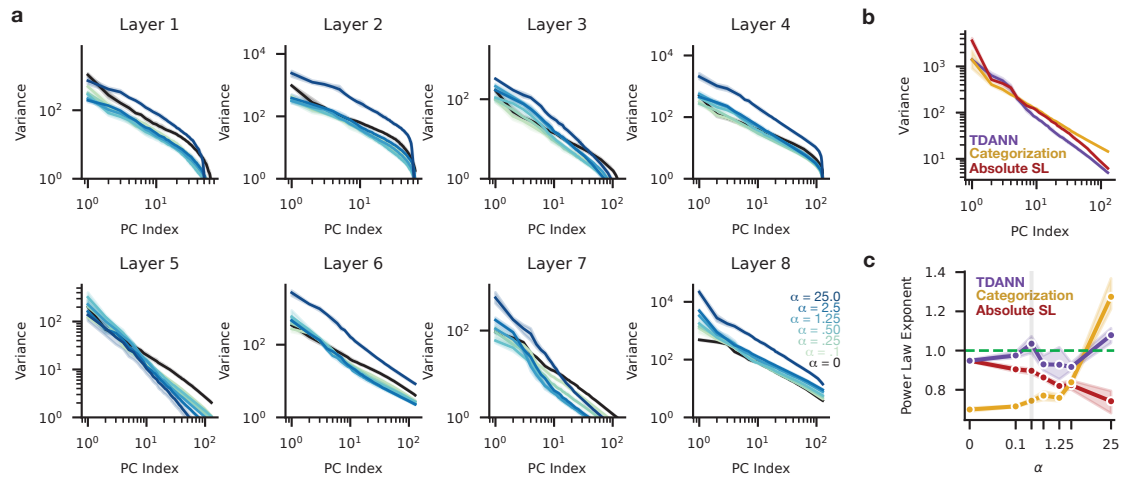


**Figure S13. Dimensionality of model unit populations as a function of training objective and  $\alpha$**  (a) Variance explained by each principal component (PC) for each layer of TDANNs trained at different levels of the spatial weight magnitude  $\alpha$ . Components computed from responses to 10,000 images from the NSD [1]. (b) Variance explained by each principal component in the VTC-like layer of models trained with  $\alpha = 0.25$  and different objectives. (c) Power law coefficient fit to eigenspectra from the VTC-like layer of models trained with  $\alpha = 0.25$  and different objectives.

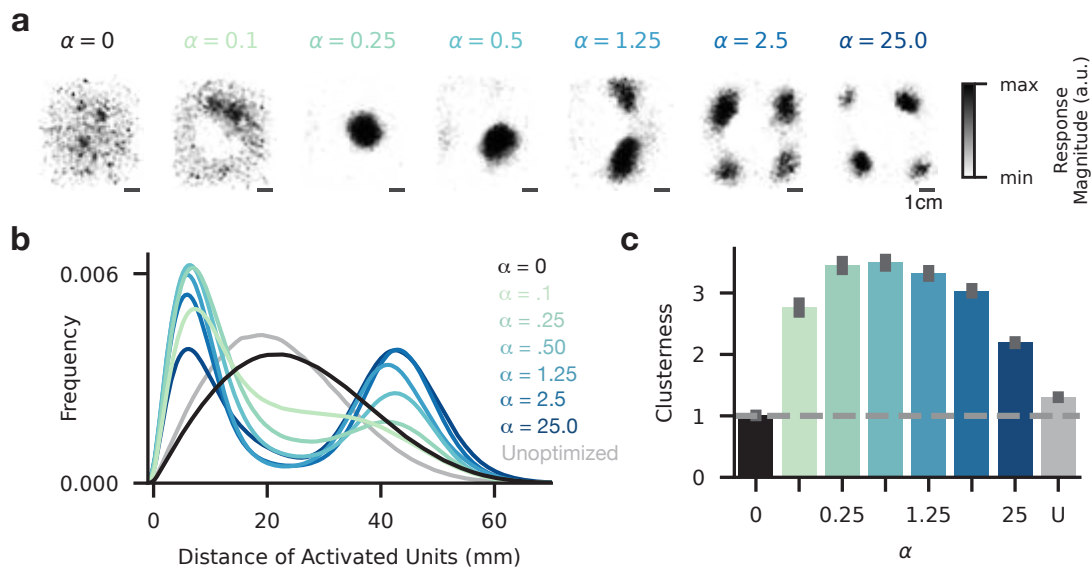


**Figure S14. Clustering of responses to natural images as a function of  $\alpha$**  (a) Strength of activation in the TDANN VTC-like layer to an arbitrarily-selected natural image, for models trained at different levels of the spatial weight ( $\alpha$ ). (b) Probability density function of pairwise distances between pairs of activated units for each model type, computed over repeated presentations of different natural images. Curve color indicates the level of the spatial weight ( $\alpha$ ) that model was trained with. (c) Clusterness, measured as the increase in unit density above the chance of value (dashed line: 1.0). Error bars: 95% CI over different random initial model seeds and images used to generate responses. ANOVA:  $F(7,32) = 70.5, p < 10^{-16}$ , post-hoc Tukey's tests: significantly lower clusterness for  $\alpha = 0$  and Unoptimized models compared to models with  $\alpha > 0$ , all post-hoc  $ps < .001$ .

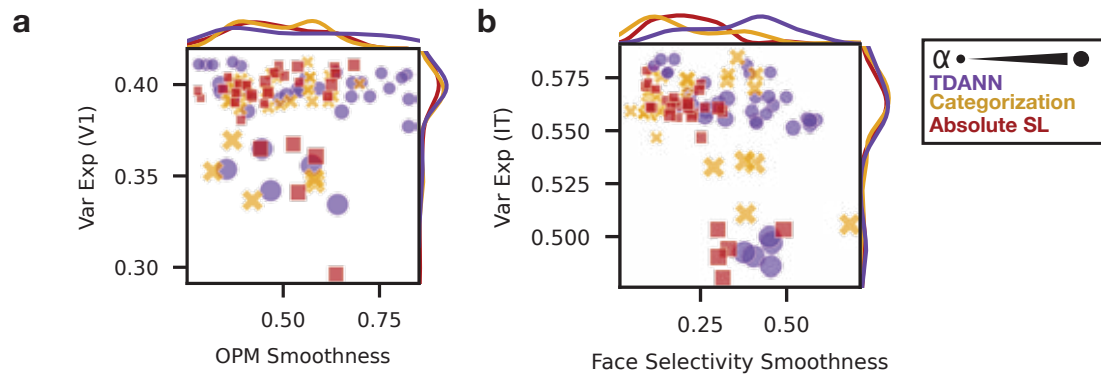


**Figure S15. Prediction of neural firing rates with linear regression compared against topographic map smoothness (a)** Models trained at different levels of  $\alpha$  (represented by dot size) and with different objectives compared in their capacity to predict macaque V1 firing rates (Var Exp) and the smoothness of their orientation preference maps. **(b)** As in (a), but for prediction of firing rates in macaque inferotemporal cortex (IT) and smoothness of face selectivity maps. No difference in variance explained when  $\alpha < 25$ , all pairwise  $p$ s from Mann-Whitney tests  $p > 0.42$ .

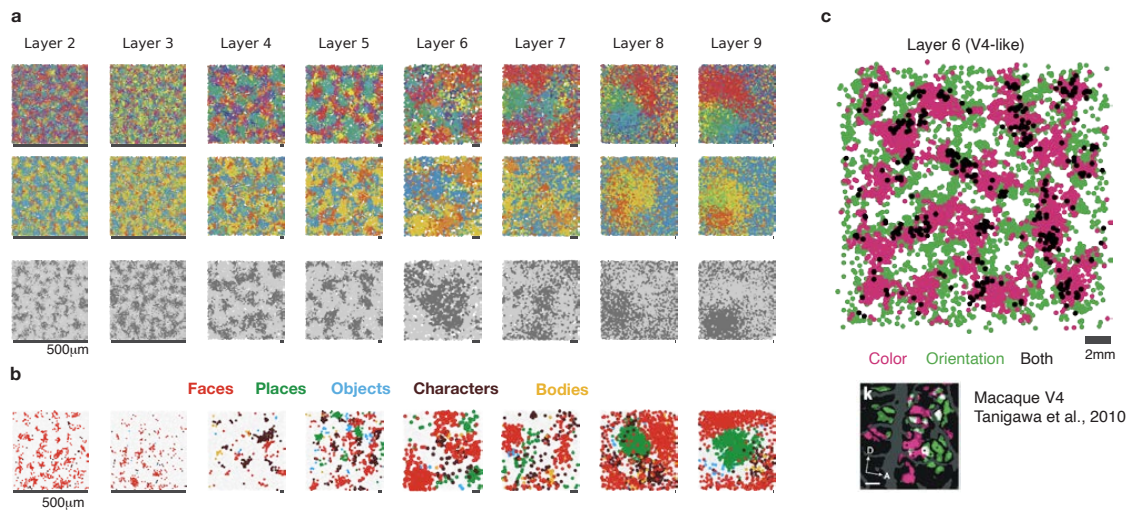


**Figure S16. Topographic maps in each layer of a representative TDANN model. (a)** Orientation, spatial frequency, and chromatic preference maps in each layer. Plotting conventions as in Figure 2. **(b)** Category selectivity map in each layer. **(c)** Orientation and color selectivity in the V4-like model layer. Units in magenta are selective for color and not orientation, units in green are selective for orientation and not color, and units in black are selective for both orientation and color. Similar data in macaque V4 is shown in the inset at bottom right (from [12]).

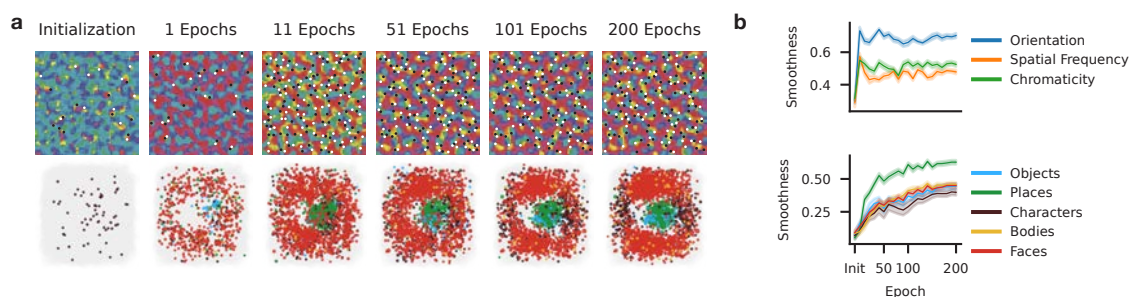


**Figure S17. Topographic maps in a representative TDANN throughout training. (a)** OPMs in the V1-like layer at initialization (left), and after 1, 11, 51, 101, and 200 epochs of training. **(b)** Category selectivity maps in the VTC-like model layer at each timepoint. **(c)** Smoothness as a function of training step for orientation, spatial frequency, and color preference maps. Smoothness peaks early then plateaus. **(d)** Selectivity of category selectivity maps for each fLoc category. Smoothness increases throughout training.

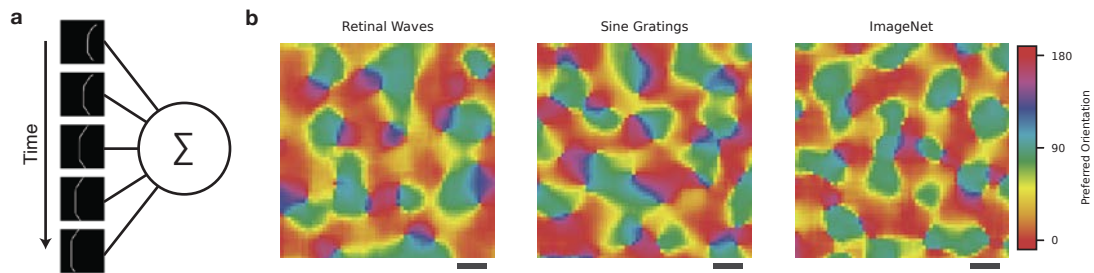


**Figure S18. Simulated retinal waves can drive unit-to-unit correlations comparable to static sine gratings. (a)** Five example frames from a simulated retinal wave movie. The responses to each frame are integrated to compute the mean response to each wave. **(b)** OPMs created by post-hoc organization of units in the V1-like layer of a Task Only SimCLR model, when the unit-to-unit correlations are computed by presenting retinal wave movies (left), a dataset of sine gratings (middle), or natural images (right). Scale bar: 2mm.

## References

- 1265
- 1266 1. Allen, E. J., St-Yves, G., Wu, Y., Breedlove, J. L., Prince, J. S., Dowdle, L. T., Nau, M., Caron, B., Pestilli,  
1267 F., Charest, I., Hutchinson, J. B., Naselaris, T., and Kay, K. A massive 7T fMRI dataset to bridge cognitive  
1268 neuroscience and artificial intelligence. *Nat. Neurosci.*, 25(1):116–126, Jan. 2022.
- 1269 2. Cadena, S. A., Denfield, G. H., Walker, E. Y., Gatys, L. A., Tolias, A. S., Bethge, M., and Ecker, A. S. Deep  
1270 convolutional models improve predictions of macaque V1 responses to natural images. *PLoS Comput. Biol.*, 15  
1271 (4):e1006897, Apr. 2019.
- 1272 3. Dapello, J., Marques, T., Schrimpf, M., Geiger, F., Cox, D. D., and DiCarlo, J. J. Simulating a primary visual  
1273 cortex at the front of CNNs improves robustness to image perturbations. June 2020.
- 1274 4. Ge, X., Zhang, K., Gribizis, A., Hamodi, A. S., Sabino, A. M., and Crair, M. C. Retinal waves prime visual motion  
1275 detection by simulating future optic flow. *Science*, 373(6553), July 2021.
- 1276 5. Jones, J. P. and Palmer, L. A. An evaluation of the two-dimensional Gabor filter model of simple receptive fields  
1277 in cat striate cortex. *J. Neurophysiol.*, 58(6):1233–1258, Dec. 1987.
- 1278 6. Kim, J., Song, M., Jang, J., and Paik, S.-B. Spontaneous Retinal Waves Can Generate Long-Range Horizontal  
1279 Connectivity in Visual Cortex. *J. Neurosci.*, 40(34):6584–6599, Aug. 2020.
- 1280 7. Kong, N. C. L., Margalit, E., Gardner, J. L., and Norcia, A. M. Increasing neural network robustness improves  
1281 match to macaque V1 eigenspectrum, spatial frequency preference and predictivity. *PLoS Comput. Biol.*, 18  
1282 (1):e1009739, Jan. 2022.
- 1283 8. Majaj, N. J., Hong, H., Solomon, E. A., and DiCarlo, J. J. Simple Learned Weighted Sums of Inferior  
1284 Temporal Neuronal Firing Rates Accurately Predict Human Core Object Recognition Performance. *Journal  
1285 of Neuroscience*, 35(39):13402–13418, 2015.
- 1286 9. Mehrer, J., Spoerer, C. J., Jones, E. C., Kriegeskorte, N., and Kietzmann, T. C. An ecologically motivated image  
1287 dataset for deep learning yields better models of human vision. *Proc. Natl. Acad. Sci. U. S. A.*, 118(8), Feb.  
1288 2021.
- 1289 10. Schrimpf, M., Kubilius, J., Lee, M. J., Ratan Murty, N. A., Ajemian, R., and DiCarlo, J. J. Integrative  
1290 Benchmarking to Advance Neurally Mechanistic Models of Human Intelligence. *Neuron*, Sept. 2020.
- 1291 11. Stringer, C., Pachitariu, M., Steinmetz, N., Carandini, M., and Harris, K. D. High-dimensional geometry of  
1292 population responses in visual cortex. *Nature*, 571(7765):361–365, July 2019.
- 1293 12. Tanigawa, H., Lu, H. D., and Roe, A. W. Functional organization for color and orientation in macaque V4. *Nat.  
1294 Neurosci.*, 13(12):1542–1548, Dec. 2010.